catalysts

MDPI

Article

Role of N-Doping and O-Groups in Unzipped N-Doped CNT Carbocatalyst for Peroxomonosulfate Activation: Quantitative Structure–Activity Relationship

Kadarkarai Govindan [1], Do-Gun Kim [2] and Seok-Oh Ko [1,*]

[1] Environmental System Laboratory, Department of Civil Engineering, Kyung University (Global Campus), Giheung-Gu, Yongin-Si 16705, Korea; govindanmu@khu.ac.kr
[2] Department of Environmental Engineering, Sunchon National University, 255 Jungang-ro, Suncheon-Si 57922, Korea; dgkim@scnu.ac.kr
* Correspondence: soko@khu.ac.kr

Abstract: We examined the relationship between the intrinsic structure of a carbocatalyst and catalytic activity of peroxomonosulfate (PMS) activation for acetaminophen degradation. A series of nitrogen-doped carbon nanotubes with different degrees of oxidation was synthesized by the unzipping method. The linear regression analysis proposes that pyridinic N and graphitic N played a key role in the catalytic oxidation, rather than pyrrolic N and oxidized N. Pyridinic N reinforce the electron population in the graphitic framework and initiate the non-radical pathway via the formation of surface-bound radicals. Furthermore, graphitic N forms activated complexes (carbocatalyst-PMS*), facilitating the electron-transfer oxidative pathway. The correlation also affirms that -C=O was dominantly involved as a main active site, rather than -C-OH and -COOH. This study can be viewed as the first attempt to demonstrate the relationship between the fraction of N-groups and activity, and the quantity of O-groups and activity by active species (quenching studies) was established to reveal the role of N-groups and O-groups in the radical and non-radical pathways.

Keywords: N-doped CNTs; PMS activation; N-groups–activity relationship; O-groups–activity relationship

Citation: Govindan, K.; Kim, D.-G.; Ko, S.-O. Role of N-Doping and O-Groups in Unzipped N-Doped CNT Carbocatalyst for Peroxomonosulfate Activation: Quantitative Structure–Activity Relationship. *Catalysts* **2022**, *12*, 845. https://doi.org/10.3390/catal12080845

Academic Editors: Gassan Hodaifa, Antonio Zuorro, Joaquín R. Dominguez, Juan García Rodríguez, José A. Peres and Zacharias Frontistis

Received: 7 July 2022
Accepted: 26 July 2022
Published: 1 August 2022

1. Introduction

In environmental remediation, metal-free carbocatalyst-based advanced oxidation processes (AOPs) with persulfates (peroxomonosulfate (PMS) and peroxodisulfate (PDS)) have received increasing attention as sustainable alternatives to metal-based AOPs [1–4]. Carbocatalysts, with a high specific surface area, unique charge carrier mobility, low mass-transfer resistance, and low-dimensional structure, have proven to be efficient in various heterogeneous catalytic processes [5–7]. Now-a-days, diverse strategies have been explored to activate PMS [8] because an asymmetric chemical structure of PMS (HSO_5^-) is believed to be effectively activated by carbocatalysts [9,10], rather than symmetric structure PDS activation [11–13].

Carbocatalyzed PMS activation and catalytic oxidation involves free radical pathways and non-free radical pathways [1,2,4]. Free radical oxidative pathways are mostly ascribed to the generation of $SO_4^{\bullet -}$, $^{\bullet}OH$ and $O_2^{\bullet -}$. Carbocatalysts activate PMS via the electron-conduction mechanisms, which can break the O-O bond in PMS to form free radicals. $SO_4^{\bullet -}$ is considered to be a more efficient oxidative free radical than $^{\bullet}OH$. $SO_4^{\bullet -}$ has higher oxidation potential (2.7–3.1 V) and longer half-life time (3.4×10^{-5} s) than $^{\bullet}OH$ with a low oxidation potential (1.8–2.7 V) and shorter half-life time (2×10^{-8} s) [14,15]. Furthermore, $SO_4^{\bullet -}$-mediated oxidation exhibits good catalytic efficiencies in a wide range of solutions of pH 3–9 [16]. Non-free radical pathways are predominantly attributed to the formation of singlet oxygen ($^1O_2$) [17,18], electron-transfer based oxidation [19], formation of surface-bound complexes [20], and surface-bound- $SO_4^{\bullet -}$ [21,22]. Generally, $^1O_2$ has

a mild oxidation potential (0.65 V), so that the reactivity of $^1O_2$ is also relatively lower than those of $SO_4^{\bullet -}$ and $^{\bullet}OH$ [23]; however, $^1O_2$ is more selective to electron-rich organic compounds [24,25]. Electron-transfer mechanism occurs when the carbocatalyst surface acts as an electron-bridge (e^- acceptor) to accelerate the electron transfer from organic pollutants (e^- donor) to PMS molecules adsorbed on the catalyst surfaces. Importantly, the non-radical pathways can also sustain excellent reactivity in complex aqueous matrices, such as wide pH conditions and the presence of various co-existing anions and natural organic matters [9].

In contemporary times, carbon nanotubes (CNTs) have demonstrated to be more efficient in PMS activation and degradation of various organic compounds [19,26–30]. CNT, with a peculiar sp^2-hybridized π conjugation, along with low level defects and limited oxygen-containing functional groups, can appreciably accelerate the catalytic activity. In fact, oxygen functional groups, including hydroxyl (-OH), carbonyl (-C=O) and carboxyl (-COOH), in the graphitic network are very important for PMS activation [1,31]. In addition, the proper modification of CNT surfaces by hetero-atom doping has shown enhanced catalytic performances [16]. That is, the N-doping on CNTs can create novel catalytic active sites, good charge distribution of neighboring carbon atoms in the conjugated sp^2-carbon network, and thus induces a high chemical potential for catalytic reactions [16]. Recent investigations demonstrated that N-doping can establish electron-rich Lewis basic sites, including boundary N (pyridinic N, pyrrolic N), substitutional N (graphitic N), and oxidized N (Table S1) [32–41]. In addition, N-doping can also create oxygen functional groups (C-OH, C=O, and COOH) in the carbon framework, which also shows good catalytic performances. A few studies stated that the C=O group profoundly participated in PMS activation among the oxygen-containing functional groups [33,35].

The quantitative structure–catalytic activity relationship in NCNT/PMS has been explored to reveal the dominant species for PMS activation [34]. This study demonstrates that graphitic N in NCNT has a major role in PMS activation and facilitates non-radical oxidative pathways through NCNT–PMS* activation complexes. However, the catalytic activity of N-groups has not been explored based on the reactive oxidative species (classical quenching studies). Similarly, quantitative correlation between oxygen-containing functional groups and catalytic activity in NCNT/PMS is of fundamental importance to reveal key active oxygen groups for PMS activation. So far, the fraction of oxygen groups-activity correlation has not been reported to interpret the key active oxygen functional groups in the NCNT/PMS system.

Therefore, to explore the relationship between oxygen functional groups and catalytic activity in the NCNT/PMS system, four different NCNT materials functionalized with distinct oxygen contents were prepared through different degrees of oxidation. Furthermore, this was the first attempt to rationalize the quantitative structure–catalytic activity relationship based on the scavenging of radical and non-radical oxidative pathways by classical quenching studies. Additionally, the relationship between the intrinsic structure of N-dopants and catalytic performance was also analyzed to unveil the role of N species in NCNT/PMS catalytic activity. Radical and non-radical reactive species were determined through classical quenching study, as well as by EPR analysis. The quenching experiments were comprehensively performed with eight different quenching agents and the catalytic activity of each radical and non-radical species was rationalized.

2. Results and Discussion

2.1. Structure Characterizations

Figure S1a displays the XRD spectra of pristine CNT, NCNT, and Uz-NCNTs. The strong diffraction peak at around 25.93° is ascribed to the (002) reflection of the hexagonal graphitic structure. N-doping (NCNT) did not noticeably change the (002) diffraction; however, the main graphitic peak position gradually decreased from 25.93° to 25.87, 25.51, and 25.27°, respectively. On the other hand, the interlayer distance of 3.43 nm of CNT/NCNT slowly increased to 3.44, 3.49 and 3.52 for Uz-NCNT-2, Uz-NCNT-4 and Uz-NCNT-8, re-

spectively. It suggests that the chemical oxidation can successively intensify the C-C bond formation and disorder the sp^2-C conjugation. Furthermore, the N-doping and chemical oxidation create defective sites (edges and vacancies) and can also establish oxygen-containing functional groups in the main graphitic network [33]. This surface modification tends to increasingly broaden the (002) diffraction peak, which substantiates the decreased graphitic degree of Uz-CNTs.

Raman spectra of the derived carbocatalysts are presented in Figure S1b. The characteristic D-band, G-band, and 2G-band of CNT were observed around 1347–1359, 1585–1612 and 2698–2732 cm^{-1}, respectively. The D-band at 1347, 1353, and 1359 cm^{-1}, and the G-band at 1501, 1612, and 1608 cm^{-1} were also noticed for Uz-NCNT-2, Uz-NCNT-4, and Uz-NCNT-8, respectively. The integrated intensity ratio of the D-band versus the G-band (I_D/I_G) is a substantial factor in determining the defect and deformation level. Table S2 shows that the I_D/I_G value of NCNT (1.03) is higher than CNT, verifying that considerable defective sites originate in the well-organized sp^2-carbon network by N-doping. The I_D/I_G value further increased for Uz-NCNT-2 (1.08) and Uz-NCNT-4 (1.13), which shows that more disorders and defective sites were established in the carbon network with the increasing oxidation levels. However, the I_D/I_G decreased to 0.96 for Uz-NCNT-8 as the degree of oxidation increased more (8 g $KMnO_4$ addition). This may be possibly due to the formation of abundant oxygenated functional groups in the carbon lattice, which could disrupt the vacancies and break the chemical bonds in the graphitic network [42]. Moreover, the intensity of the 2D-band at 2703 cm^{-1} also diminished as the amount of oxidizing agent ($KMnO_4$) increased. It implies that the chemical oxidation employed with 2, 4 and 8 g of $KMnO_4$ brings more boundaries, sp^3 domains or vacancies and disorders into the carbon network, along with edges [38].

Figure S2a shows that the absorption peak at 273 nm (CNT, and NCNT) is attributed to the π-π* excitation of the graphitic sp^2-C network. This π-π* absorption peak shifted substantially to 230 nm for Uz-CNTs. This crucial blue-shift informs us that the homogenous sp^2-C=C conjugation is broken, and sp^3-C-C domains are formed on the carbocatalyst surface by chemical oxidation. Figure S2b exhibits FT-IR spectra of the carbocatalyst. It displays limited oxygenate functional groups that exist on the CNT, as well as NCNT surfaces. A few evident bands visibly appeared with the Uz-CNT samples. In particular, the bands at around 1980 and 1891 cm^{-1} correspond to the asymmetric and symmetric stretching vibrations of the C-H bond, while the bands at around 1717, 1580, 1389, 1167 and 1038 cm^{-1} are ascribed to the -C=O, -C=N/-C=C, -C-OH, -C-N, and -C-O stretching vibrations, respectively [43].

2.2. Specific Surface Area and Chemical Status

N_2 sorption isotherm and BJH pore size distribution profiles are shown in Figure S3. N_2 adsorption/desorption isotherm results of all the samples (except Uz-NCNT-4) reveal a Type IV isotherm with a H1-type hysteresis loop when P/P_0 = 0.4–0.9. Uz-NCNT-4 exhibits a Type IV isotherm with a H3-type. Type H1 hysteresis implies that the catalyst channels have uniform pore sizes and shapes, while the type H3 hysteresis proposes that the catalyst (Uz-NCNT-4) contains a very wide distribution of pore sizes [44,45]. The evident peak between 3 and 5 nm in Figure S3f states that the synthesized carbocatalysts primarily consist of mesoporous structures (>2 nm). As shown in Table S3, the BET surface area 206.41 $m^2\ g^{-1}$ (CNT) is not substantially changed by N doping (207.06 $m^2\ g^{-1}$, NCNT), but it is gradually reduced to 163.04 $m^2\ g^{-1}$ (Uz-NCNT-2), 140.72 $m^2\ g^{-1}$ (Uz-NCNT-4) and 4.41 $m^2\ g^{-1}$ (Uz-NCNT-8) with increasing dosages of oxidizing agent ($KMnO_4$). The decrease in BET surface area is probably due to the collapse of the carbon skeleton structure and crinkled layers during the oxidation processes. The high loss of surface area with Uz-NCNT-8 is possibly due to the intense stacking effect, resulting from strong hydrogen bonding between the oxygen functionalities on the catalyst surface. X. Duan and coworkers reported that heteroatom (N, P and S) doping into graphene greatly reduces the specific surface area due to formation of a crinkled layer and stacking effect [46,47].

The chemical compositions of the nitrogen-doped carbocatalysts were examined by XPS and are displayed in Figure S4 and Table S4. As shown in Figure S4b, the N 1s characteristic peak is noticed at around 399.9–400.8 eV, indicating that N atoms were successively introduced into the carbocatalyst. The analysis also shows the N content of 0.93, 1.07, 1.04, and 0.62% is noticed in NCNT, Uz-NCNT-2, Uz-NCNT-4 and Uz-NCNT-8, respectively (Table 1). The high resolution N 1s spectrum in a specific range (392–410 eV) was deconvoluted into four N-groups, such as pyridinic N, pyrrolic N, graphitic N or substitutional N, and oxidized N (Figure S4c–f). The deconvoluted peak center, peak area and total area of the respective sample are provided in Table 1. Each peak area was divided by the total area of the specific N 1s spectrum and calculated the fraction of N-dopants. Table 1 denotes that the pyridinic N and graphitic N contents were progressively enriched from NCNT to Uz-NCNT-2 and Uz-NCNT-4, and then drastically reduced for Uz-NCNT-8. In contrast, pyrrolic N content decreased from NCNT to Uz-NCNT-2, and Uz-NCNT-4 and increased at Uz-NCNT-8. On the other hand, oxidized N content greatly decreased from NCNT to Uz-NCNT-4 and completely vanished for Uz-NCNT-8. The analysis concludes that the amount of oxidizing agent significantly governs the N-dopants' levels.

Table 1. Atomic percentages of elements in the carbocatalysts were obtained from XPS analysis.

Carbocatalysts	N/at. %	N/at. %			
		Pyridinic N	Pyrrolic N	Graphitic N	Oxidized N
CNT	NA	0.00	0.00	0.00	0.00
NCNT	0.93	0.06	0.28	0.35	0.32
Uz-NCNT-2	1.07	0.13	0.13	0.53	0.20
Uz-NCNT-4	1.04	0.18	0.18	0.72	0.05
Uz-NCNT-8	0.62	0.15	0.67	0.18	0.00
	C at. %	**O at. %**	**O/at. %**		
			C-O	**C=O**	**COOH**
CNT	99.11	0.89	0.63	0.37	0
NCNT	96.04	3.04	0.21	0.58	0.21
Uz-NCNT-2	77.43	21.5	0.22	0.54	0.24
Uz-NCNT-4	74.39	24.58	0.08	0.59	0.33
Uz-NCNT-8	67.22	32.16	0.10	0.45	0.46

Table 1 also indicates that the oxygen atomic percentage steadily increased from 0.89 (CNT) to 3.04, 21.5, 24.58, 32.16% with NCNT, Uz-NCNT-2, Uz-NCNT-4 and Uz-NCNT-8, respectively. It confirms that extending oxidation levels establish more oxygen-containing functional groups in the carbon network. High resolution O 1s spectrum between 526 and 541 eV was deconvoluted into five major peaks, which are related to the hydroxyl group (C-O), carbonyl group (C=O), and carboxyl group (COOH) (Figure S5 and Table S5). Table 1 presents the amount of C-O group, 0.63 at. % (CNT), which steadily decreased to 0.21, 0.22, and 0.08 with NCNT, Uz-NCNT-2 and Uz-UNCT-4, respectively, although it slightly fluctuated to 0.10 at. % for Uz-NCNT-8. In contrast, the C=O group content increased from 0.37 at. % (CNT) to 0.58 for NCNT and then it fluctuated to 0.54, 0.59, and 0.45 at. % with increasing oxidizing power of 2, 4 and 8 g $KMnO_4$, respectively. The lower C=O fraction for Uz-NCNT-8 may be due to the transformation of C=O into the -COOH group at a higher degree of oxidation level. The oxidation process employed $KMnO_4$ in concentrated H_2SO_4 as an oxidizing agent; this can generate the strong oxidizer Mn_2O_7. This Mn_2O_7 oxidizer is able to oxidize the carbonyl groups in aldehyde or benzoquinone structures on carbocatalyst surfaces and converts them to -COOH [48–50]. Thus, the amount of -COOH gradually increased with the degree of oxidation level in this study. The analysis affirms that the $KMnO_4$ dosage crucially controlled the formation of oxygen-containing functional groups.

2.3. Catalytic Performance

2.3.1. Role of N-Doping on Catalytic Performances

Catalytic performance of all carbocatalysts was examined using constant pollutant concentration (C_{ACP} = 10 mg L^{-1}), and PMS dosage (C_{PMS} = 0.5 mM) with $pH_0 = 7 \pm 0.3$ and is presented in Figure 1a,b. It was found that ACP degradation profiles for all catalysts were well fitted with the first-order kinetic model. The ACP degradation rate constant, k_1 (ACP) = 4.37 × 10^{-4} s^{-1}, for CNT is enhanced to 18.4 × 10^{-4} s^{-1} for NCNT, validating that the surface modification of CNT by nitrogen doping greatly increases the catalytic activity. The k_1 (ACP) of NCNT is further increased to 22.05 × 10^{-4}·s^{-1} (Uz-NCNT-2), and 28.35 × 10^{-4} s^{-1} (Uz-NCNT-4) with the increase in the degree of oxidation level, respectively. However, the k_1 (ACP) for Uz-NCNT-8 is relatively lower than k_1 for Uz-NCNT-2 and Uz-NCNT-4. This might be due to the presence of the low fraction of N (0.62 at. %) in Uz-NCNT-8, compared to Uz-NCNT-2 (1.07 at. %) and Uz-NCNT-4 (1.04 at. %). Furthermore, the graphitic N fraction is also substantially reduced for Uz-NCNT-8. The graphitic N can greatly influence the electron transfer ability among N dopants, because it can readily alter the charge distribution of adjacent carbon atoms due to the electronegativity [27]. It is also noted that the existence of abundant pyrrolic N (0.67 at. % for Uz-NCNT-8) adversely influences the catalytic activity of the carbocatalyst. Typically, a pyrrolic N atom is attached to a five membered pentagonal ring and contributes two *p*-electrons to the π system, increasing the electron density of the main graphitic layer [16]. However, the lone pair of electrons in the sp^2 orbital is parallel to the sp^2 orbital of adjacent C [51]. As a result, the lone pair of electrons readily contributes to the delocalization and reinforces the density of the graphitic network, rather than transporting electrons to the adsorbed organics and/or PMS. Due to the spatial arrangement of sp^2 pyrrolic N, the adsorption of organics or PDS on the pyrrolic ring is hindered.

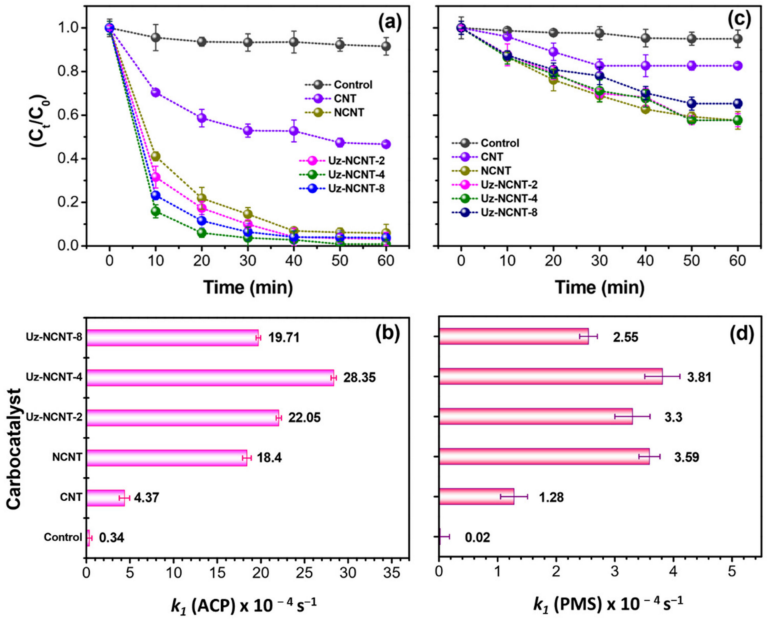

Figure 1. (**a**) ACP degradation profile versus time and (**b**) first-order kinetic rate constant, k_1 (ACP). (**c**) PMS decomposition profile versus time and (**d**) k_1 (PMS). Experimental conditions C_{ACP} = 10 mg L^{-1}, $C_{Catalyst}$ = 100 mg L^{-1}, C_{PMS} = 0.5 mM and $pH_0 = 7 \pm 0.3$.

To evaluate the role of each N species on the catalytic performance, the regression analysis was applied between N-contents and k_1 (ACP). In Figure 2a, high linear correlation was obtained with pyridinic N (R^2 = 0.9219) and graphitic N (R^2 = 0.8891). Meanwhile, low correlations were obtained for pyrrolic N (R^2 = 0.1363) and oxidized N (R^2 = –0.0055). Similarly, the PMS decomposition rate constants, k_1 (PMS), of all carbocatalysts were also

examined and are displayed in Figure 1c,d. It implies that the k_1 (PMS), 1.28×10^{-4} s^{-1} for CNT, is substantially enhanced with NCNT (3.59×10^{-4} s^{-1}), and slightly fluctuates for Uz-NCNT-2 (3.3×10^{-4} s^{-1}). This may be due to the crinkled graphitic layer during the chemical oxidation process. Then, k_1 (PMS) increased for Uz-NCNT-4 (3.81×10^{-4} s^{-1}) and decreased for Uz-NCNT-8 (2.55×10^{-4} s^{-1}). Furthermore, the relationship between k_1 (PMS) and N-dopants in Figure 2b exhibits a reasonable correlation ($R^2 = 0.7014$) with graphitic N, affirming that graphitic N appreciably promotes PMS activation, rather than other boundary Ns (i.e., pyrrolic N and oxidized N). Although graphitic N seems to play a main role in the catalytic system via PMS activation (0.8891 with k_1 (ACP) and 0.7014 with k_1 (PMS)), pyridinic N also slightly outperforms the other N-dopants. This may be attributed to the fact that pyridinic N has a lone pair of electrons considered as a Lewis basic site, which can effectively enhance the electron population of the main graphitic layer and improve the catalytic activity [52]. Moreover, the substitutional N (graphitic N) can also break the uniform sp^2-hybridized π-conjugations at the carbon periphery. The higher electronegative N atom (graphitic N) can induce a positive charge to adjacent carbon atoms through charge transfer. As a result, the positively charged sites can enhance the PMS adsorption and weaken the peroxide bond (O-O) in $HO\text{-}SO_4^-$, generating reactive oxidative species [34,36].

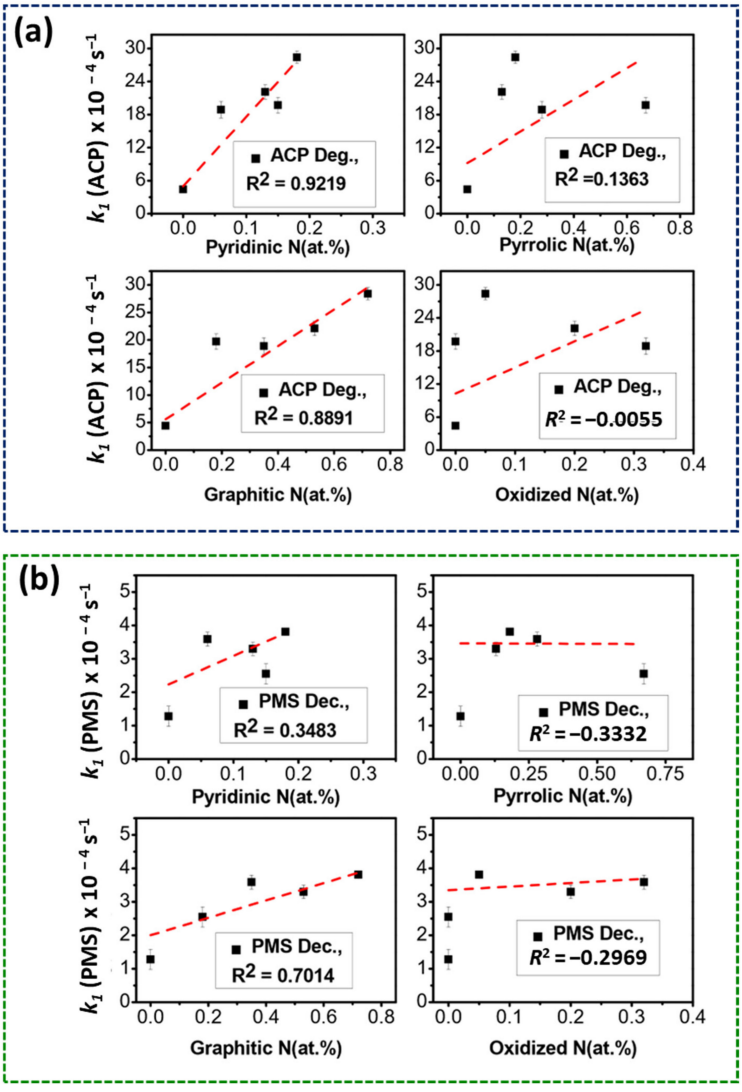

Figure 2. Role of N-content and specific N-constituent in k_1 (ACP) (**a**), and k_1 (PMS) (**b**). Experimental conditions C_{ACP} = 10 mg L^{-1}, $C_{Catalyst}$ = 100 mg L^{-1}, C_{PMS} = 0.5 mM and $pH_0 = 7 \pm 0.3$.

2.3.2. Role of Oxygen Functionalities on Catalytic Performances

Three oxygen-containing functional groups (C-O, C=O, and -COOH) and the amount of oxygen groups are detected from O 1s XPS spectra and are summarized in Table 1. To ascertain the effect of the O-content and three oxygen groups on catalytic performance, the k_1 (ACP)-O-content relationship was evaluated (Figure 3a,b). In Table 1, the reaction rate k_1 (ACP) gradually increased with the increasing atomic percentage of O-content from 0.89 at. % for CNT to 3.04 at. % (NCNT), 21.5 at. % (Uz-NCNT-2), and 24.58 at. % (Uz-NCNT-4). However, k_1 (ACP) decreased at 32.16 at. % of oxygen content (Uz-NCNT-8). Increasing the fraction of oxygen content could significantly enhance the electron population in the graphitic layer, which could remarkably enhance the electron transfer oxidative steps. Furthermore, the existence of a significant quantity of oxygen functional groups in the graphitic framework could also appreciably transport the electrons to PMS or organics, resulting in a higher degradation rate [53]. Nonetheless, the decrease in k_1 (ACP) for Uz-NCNT-8 may be ascribed to the existence of the many oxygen-containing functional groups, which make the electron conductivity of the graphitic layer worse by occupying the active edges and blocking the interaction between the carbocatalyst and PMS through a stereo-hindrance effect [53]. It implies that oxygen-containing functional groups crucially govern ACP degradation in CNT-based carbocatalyzed PMS systems.

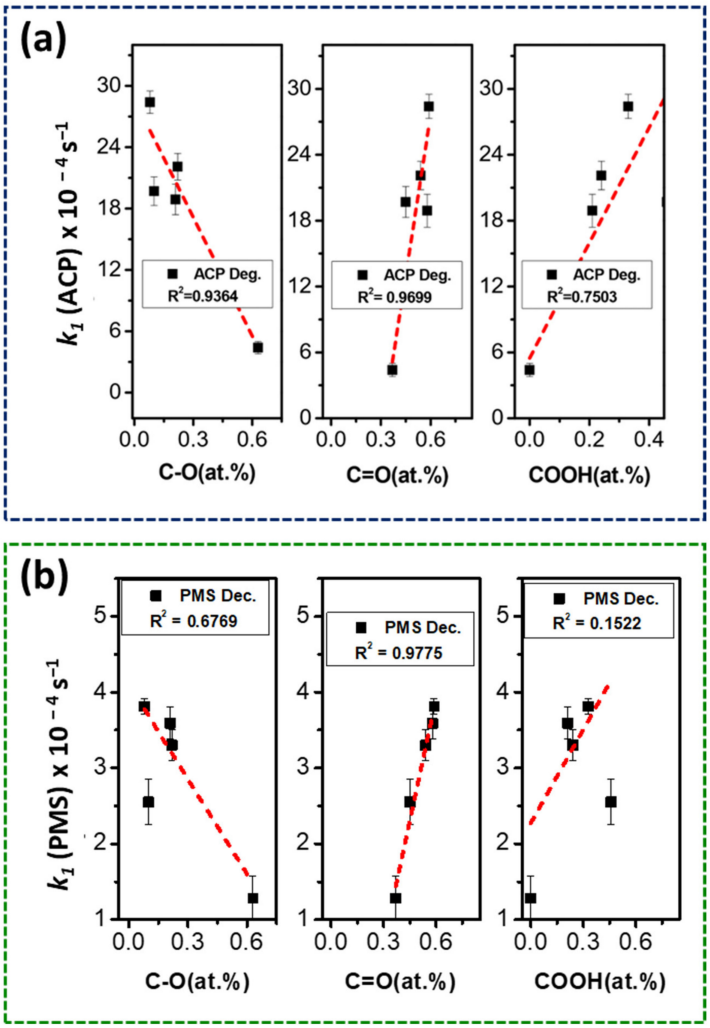

Figure 3. Role of O-contents and oxygen functionalities in k_1 (ACP) (**a**), and k_1 (PMS) (**b**). Experimental conditions C_{ACP} = 10 mg L^{-1}, $C_{Catalyst}$ = 100 mg L^{-1}, C_{PMS} = 0.5 mM and pH_0 = 7 ± 0.3.

A well fitted positive linear correlation (R^2 = 0.9699) with a -C=O group confirms that the carbonyl group at the edges is a dominant active site in the catalytic systems (Figure 3b). Recent investigations have also demonstrated that the electron-rich -C=O group is believed to be a paramount active site for PMS activation because it breaks the O-O bond in PMS into $SO_4^{\bullet -}$ and $^{\bullet}OH$ and then triggers the formation of $^1O_2$ [33,35]. Meanwhile, the correlation (R^2 = 0.7503) with the -COOH group suggests that carboxylic acid functionalities are also participating in the catalytic oxidation processes [54–56]. On the other hand, a negative linear fit for -C-O (R^2 = 0.9364) indicates that the excessive electron-donating hydroxyl groups in the main graphitic structure might be unfavorable for electron-transfer oxidation [53]. A good linear relationship between k_1 (PMS) and -C=O (R^2 = 0.9775) in Figure 3b proposes that the carbonyl groups at the reactive edges and defective sites can remarkably aid the PMS activation [33,35]. Furthermore, the poor correlation between -COOH and k_1 (PMS) indicates that the PMS adsorption did not significantly initiate -COOH. It may be due to the COOH group's spatially wide molecular structure and hindered broad molecular structure of the PMS. However, the meaningful R^2 between k_1 (ACP) and -COOH may be due to the electron-withdrawing carboxylic group altered the electron density in the graphitic structure and facilitates the electron transfer oxidative steps.

2.4. Identification of Main Reactive Oxidative Species in Carbocatalyst/PMS Systems

Typically, PMS activation by CNT-based carbocatalysts can generate diverse radical and non-radical oxidative components, as described in Equations (1)–(18). EPR was used to find the active species involved in the carbocatalyzed PMS activation systems. The spin-trapping agent TMP was employed to detect the $^1O_2$. In Figure 4a, a weak signal was observed in PMS without a catalyst because of the slow self-decomposition of PMS [57]. For all the carbocatalysts/PMS systems, a typical three-line TMP-$^1O_2$ adduct signal with equal intensities (1:1:1) was obtained. It substantiates the fact that the interaction between carbocatalysts and PMS can invariably generate $^1O_2$ to react with TMP and produces the stable adduct 2,2,6,6-tetramethyl-4-piperidnol-N-oxyl. Superoxide radical anion $O_2^{\bullet -}$ can also react with TMP to form equal intensities of three-line EPR signals [58]. Thus, to evaluate the contribution of $O_2^{\bullet -}$ in carbocatalyst/PMS systems, EPR analysis was carried out in the presence of an $^1O_2$ quencher (10 mM FFA). As shown in Figure 4b, the intensities of the three-line TMP-$^1O_2$ adduct signal are considerably diminished, corroborating that $O_2^{\bullet -}$ is also produced in carbocatalyzed PMS activation.

$$\text{CNT-C=N} + HSO_5^- \rightarrow \text{CNT-C-N}^+ + SO_4^{\bullet -} + OH^- \quad (1)$$

$$\text{CNT-C=N} + HSO_5^- \rightarrow \text{CNT-C-N}^+ + SO_4^{2-} + {}^{\bullet}OH \quad (2)$$

$$\text{C=C=N-C}_{surface}\text{-C=O} + HSO_5^- \rightarrow \text{C}_{surface}\text{-C=O}^+ + SO_4^{\bullet -} + OH^- \quad (3)$$

$$\text{C=C=N-C}_{surface}\text{-C=O} + HSO_5^- \rightarrow \text{C}_{surface}\text{-C=O}^+ + SO_4^{2-} + {}^{\bullet}OH \quad (4)$$

$$\text{C}_{surface}\text{-C=O}^+ + HSO_5^- \rightarrow \text{C}_{surface}\text{-C=O}^+ + SO_5^{\bullet -} + OH^- \quad (5)$$

$$\text{C=C=N-C}_{surface}\text{-COOH} + HSO_5^- \rightarrow \text{C}_{surface}\text{-COO}^+ + SO_4^{\bullet -} + 2OH^- \quad (6)$$

$$\text{C=C=N-C}_{surface}\text{-OH} + HSO_5^- \rightarrow \text{C}_{surface}\text{-O}^+ + SO_4^{\bullet -} + 2OH^- \quad (7)$$

$$\text{C=C=N-C}_{surface}\text{-C=O} + HSO_5^- \rightarrow \text{C}_{surface}\text{-C=O=O} + H^+ \quad (8)$$

$$\text{C}_{surface}\text{-C=O-O}^+ + SO_5^{2-} \rightarrow \text{C}_{surface}\text{-C=O} + {}^1O_2 \quad (9)$$

$$\text{C=C=N-C}_{surface}\text{-C=O} + HSO_5^- + 2OH^- \rightarrow \text{C}_{surface}\text{-C-O-O}^+ + H_2O + SO_4^{2-} \quad (10)$$

$$\text{C=C=N-C}_{surface}\text{-C-O-O}^+ + HSO_5^- + 2OH^- \rightarrow \text{C}_{surface}\text{-C=O} + {}^1O_2 + H_2O + SO_4^{2-} \quad (11)$$

$$SO_5^{2}- + HSO_5^- \rightarrow HSO_4\text{-}\ SO_4^{2}- + {}^1O_2 \quad (12)$$

$$2O_2^{\bullet -} + 2H_2O \rightarrow H_2O_2 + {}^1O_2 + OH^- \quad (13)$$

$$O_2^{\bullet -} + {}^{\bullet}OH \rightarrow {}^1O_2 + OH^- \quad (14)$$

$$HSO_5^- + e^- \rightarrow SO_4^{\bullet -} + OH^- \quad (15)$$

$$HSO_5^- + e^- \rightarrow SO_4^{2-} + {}^{\bullet}OH \quad (16)$$

$$HSO_5^- + NCNT\text{-}C \cdots \pi^+ \rightarrow SO_4^{\bullet -} + OH^- \quad (17)$$

$$HSO_5^- + NCNT\text{-}C \cdots \pi^+ \rightarrow SO_4^{2-} + {}^{\bullet}OH \quad (18)$$

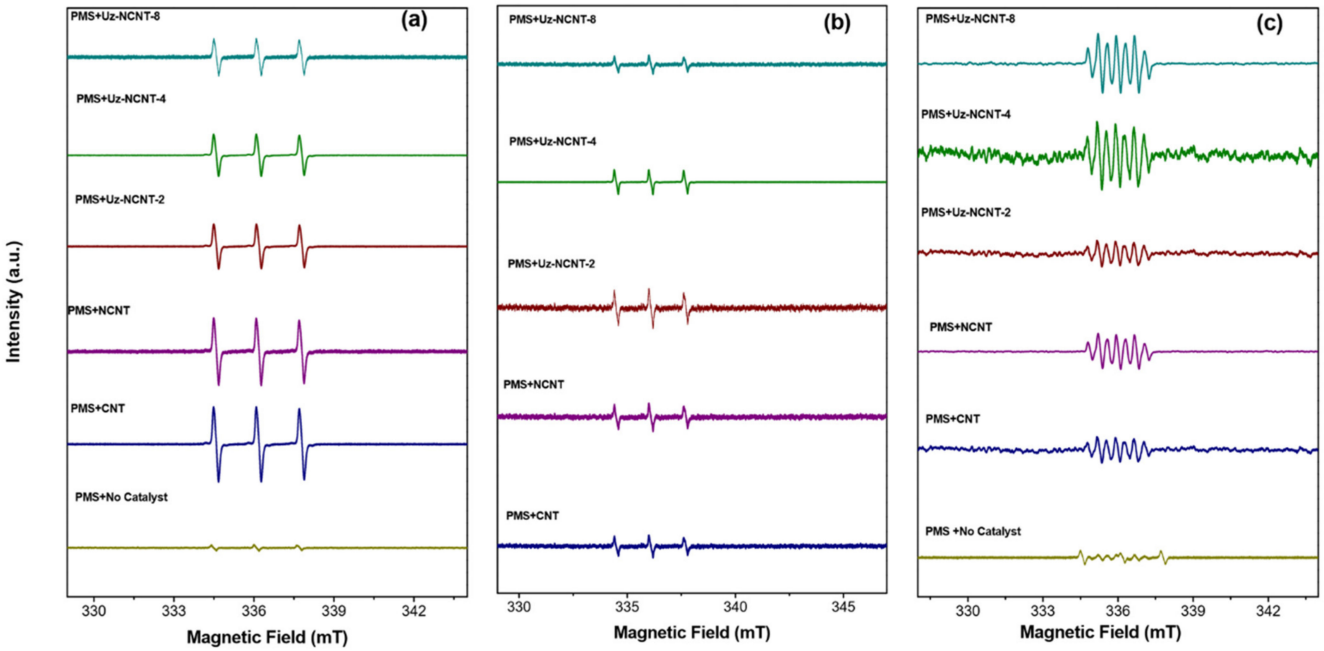

Figure 4. (**a**) EPR spectra of TMP-$^1O_2$ adducts under different carbocatalyst/PMS systems. (**b**) EPR spectra of TMP-$^1O_2$ analyzed in the presence of C_{FFA} = 10 mM, and C_{TMP} = 50 mM; (**c**) EPR spectra of DMPO-$SO_4^{\bullet -}$ and DMPO- $^{\bullet}OH$ adducts were analyzed using C_{DMPO} = 100 mM. $C_{Catalyst}$ = 10 mg L^{-1}, C_{ACP} = 10 mg L^{-1}; and C_{PMS} = 1 mM.

Other active free radicals $SO_4^{\bullet -}$ and $^{\bullet}OH$ were also identified by using an EPR, in which the spin-trapping agent 5,5-dimethyl-1-pyrroline N-oxide (DMPO) was employed to detect $SO_4^{\bullet -}$ and $^{\bullet}OH$. In Figure 4c, the weak characteristic peaks of DMPO-$^{\bullet}OH$ can be observed from PMS only. This can be ascribed to the hydrolysis of PMS that forms less $^{\bullet}OH$. In contrast, the prominent variation in the peak intensity is observed before and after the addition of the carbocatalyst, verifying that derived carbocatalysts (NCNT, Uz-NCNT-2, Uz-NCNT-4 and Uz-NCNT-8) are capable of generating $SO_4^{\bullet -}$and $^{\bullet}OH$. The reaction between $^{\bullet}OH$ and DMPO can produce a DMPO- $^{\bullet}OH$ adduct signal, with a relative intensity ratio of 1:2:1:2:1:2:1 [59,60]. This may be due to the fact that DMPO can oxidize and yield 5,5, -dimethyl-2-pyrrolidon-N-oxyl (DMPOX). The presence of a DMPOX signal in Figure 4c specifies that $^{\bullet}OH$, and $SO_4^{\bullet -}$ are consistently formed in carbocatalyst/PMS systems. This may be due to the transformation of DMPO-$SO_4^{\bullet -}$ and DMPO- $^{\bullet}OH$ adducts. A fast nucleophilic substitution reaction between highly reactive DMPO-$SO_4^{\bullet -}$ and H_2O (DMPO-$SO_4^{\bullet -}$ = 95 s in water) resulted in the rapid transformation of the DMPO-$SO_4^{\bullet -}$ adduct into DMPO-$^{\bullet}OH$. Then, DMPO- $HO^{\bullet}$ was oxidized into DMPOX through electron abstraction by $HO^{\bullet}$ and/or $SO_4^{\bullet -}$ [61]. EPR study recommends that $SO_4^{\bullet -}$and $^{\bullet}OH$ are also formed through PMS activation and contribute to ACP degradation.

2.5. Classical Quenching Studies

To further identify the reactive oxidative species that participated in the catalytic systems, classical quenching experiments were also attempted in detail. The ethanol/*tert*-

BA, and *p*-BQ were utilized to detect $SO_4^{\bullet -}$/$^{\bullet}OH$ and $O_2^{\bullet -}$, respectively [62–65], and FFA and L-His were considered as efficient quenchers to identify the $^1O_2$ [66,67]. The non-free radicals, surface-bound radicals, surface-bound activated complexes, and free flowing electrons were also evaluated using specific quenchers, such as KI, phenol, and $NaClO_4$, respectively [43,68,69]. The rate constants for the reactions between the reactive oxidative species and specific quencher are briefly described in Table 2.

The effect of quenchers on the ACP degradation profiles and observed first-order rate constants are shown in Figures S6 and S7, respectively. In general, the ACP degradation rate constant is substantially inhibited by the addition of specific quenchers, suggesting that radicals ($SO_4^{\bullet -}$/$^{\bullet}OH$ and $O_2^{\bullet -}$), $^1O_2$, non-free radicals (surface-bound radicals, surface-bound complexes, and free flowing electrons) are intrinsically involved in the catalytic system. In particular, the high inhibition rate with the $^1O_2$ quencher (L-His, FFA) in CNT/PMS and NCNT/PMS proposes that $^1O_2$ based-oxidation process led to ACP degradation. It may be because the PMS activation by the carbocatalyst (CNT and NCNT) with a smaller number of oxygen groups was limited, resulting in the lower amount of free radical formation. Furthermore, the adsorption of organics by the carbocatalyst was ascribed to the π–π interactions and electrostatic interactions between the electron donor (ACP) and electron acceptor (catalyst). Subsequently, the organic contaminant was degraded via the electron-transfer mechanism in the surface of the graphitic layer (i.e., non-radical oxidative pathway) [42]. In contrast, the radical quenchers (ethanol, *tert*-BA and *p*-BQ) and non-radical quenchers ($NaClO_4$ and phenol) greatly hampered the ACP degradation rate with the oxidized NCNTs (Uz-NCNT-2, Uz-NCNT-4 and Uz-NCNT-8). The considerable number of oxygen contents in the catalyst surface can significantly enhance the electron density of the graphitic network. It can efficiently interact with the peroxo bond (-O-O-) in the PMS structure and enhance free radical generation. It is evident that free-radicals, as well as non-radical electron-transfer based oxidation, jointly facilitate ACP degradation with Uz-CNTs/PMS system.

2.5.1. Role of N-Dopants on Radical and Non-Radical Pathway

The role of N-dopants on PMS activation for ACP degradation was further rationalized based on the results in Figure S7. To investigate the relationship between N-dopants and individual oxidative species activity, the normalized inhibition ability by a specific quenching agent was calculated according to the equation given below.

$$\text{Inhibition Ability} = \frac{k_1(ACP)_C - k_1(ACP)_Q}{k_1(ACP)_C} \quad (19)$$

where $k_1(ACP)_C$ is the first-order ACP degradation rate constant for the carbocatalyst/PMS in the absence of quenchers, and $k_1(ACP)_Q$ is the ACP degradation rate constant with a specific quencher. The normalized inhibition ability with N-dopants is presented in Figures 5–7. The notable correlation of ethanol (R^2 = 0.7359) and *tert*-BA (R^2 = 0.7309) (*tert*-BA) with pyridinic N was observed in Figure 5a, while the correlation (R^2 = −0.1122) between *p*-BQ and pyridinic N-content was low. The correlation illustrates that pyridinic N substantially governs $SO_4^{\bullet -}$/$^{\bullet}OH$ formation and radical-based oxidation. This may be explained by the fact that the lone pair of electrons are in a sp^2 (pyridinic N) orbital perpendicular to the sp^2 orbitals of the adjacent carbon; thus, the pyridinic N can readily transport the non-bonded electrons to PMS and facilitate the formation of free radicals ($SO_4^{\bullet -}$/$^{\bullet}OH$) [70]. A plausible PMS activation mechanism, as described in Equations (1)–(18), suggests that no direct interaction occurs between PMS and the N-functional group to form superoxide anion radicals. Furthermore, *p*-BQ yields a good R^2 value (0.9256) with graphitic N, proving that graphitic N plays a crucial role in $O_2^{\bullet -}$ mediative oxidation. The increased inhibition ability by the $O_2^{\bullet -}$ quencher (*p*-BQ) indicates that a great number of $O_2^{\bullet -}$ contributes to efficient ACP degradation. The relationship between graphitic N and *tert*-BA seems to be that inhibition ability increased with the increasing graphitic N content, suggesting that graphitic N heavily influences the formation of $SO_4^{\bullet -}$/$^{\bullet}OH$. Figure 5

also implies that pyrrolic N and oxidized N did not appreciably participate in the radical oxidative pathway, as they show very low R^2 values with ethanol and *tert*-BA (Figure 5b,d). Figure 5a,c also imply that the low slope value between pyridinic N vs. p-BQ and graphitic N vs. p-BQ suggested that pyridinic N and graphitic N did not control the formation of $O_2^{\bullet -}$.

Table 2. The second-order rate constants for the reaction between reactive oxidative species and specific quenchers.

	Scavengers	Molecular Formula	ROS Species	Reaction Rate Constant (M^{-1} s^{-1})	References
1	Ethanol	C_2H_5OH	$SO_4^{\bullet -}$ and $^{\bullet}OH$	$k_{SO4^{\bullet -}} = 9 \times 10^8$ $k_{HO^{\bullet}} = 1.1 \times 10^6$	[63,71]
2	*tert*-Butyl alcohol	$C_4H_{10}O$	$^{\bullet}OH$	$k_{HO^{\bullet}} = 4.5 \times 10^8$	[63]
3	*p*-Benzoquinone	$C_6H_4O_2$	$O_2^{\bullet -}$	$k_{obs.} = 9 \times 10^8$	[64,65]
4	L-histidine	$C_6H_9N_3O_2$	$^1O_2$	$k_{obs.} = 3 \times 10^8$	[16,67]
5	Furfuryl alcohol	$C_5H_6O_2$		$k_{obs.} = 1.2 \times 10^8$	
6	Phenol	C_5H_5OH	Surface-bound radicals ($SO_4^{\bullet -}$ and $^{\bullet}OH$)	$k_{SO4^{\bullet -}} = 8.8 \times 10^9$ $k_{HO^{\bullet}} = 6.6 \times 10^9$	[68,69]
7	Potassium iodide	KI	Surface bound complexes	–	[72,73]
8	Sodium perchlorate	$NaClO_4$	Free electrons	–	[43]

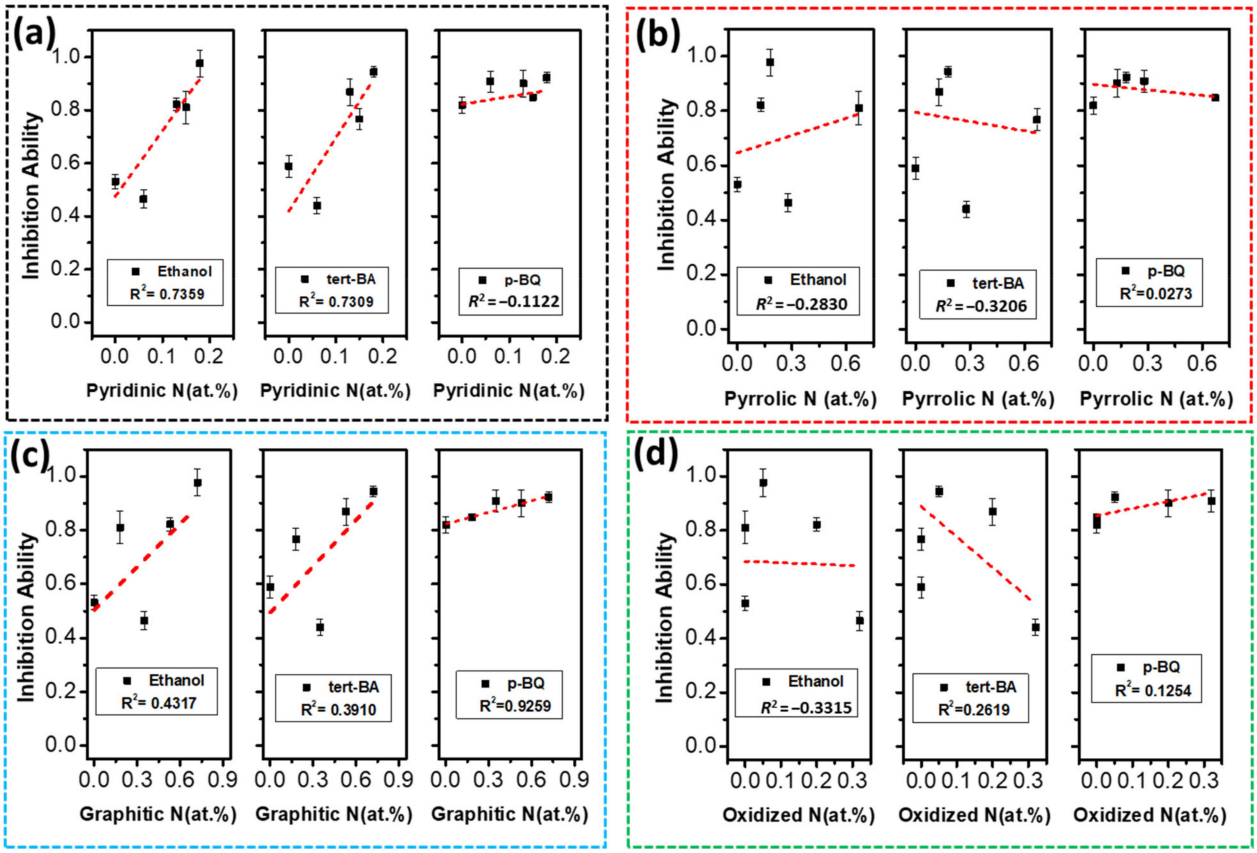

Figure 5. Role of radical ($O_2^{\bullet -}$-, $^{\bullet}OH$ and $SO_4^{\bullet -}$) quenchers on ACP degradation rate (k_1(ACP)). Correlation between k_1 (ACP) and pyridinic N (**a**), k_1 (ACP) and pyrrolic N (**b**), k_1 (ACP) and graphitic N (**c**), and k_1 (ACP) and oxidized N (**d**). Quenching studies were carried out at C_{ACP} = 10 mg L^{-1}, $C_{Catalyst}$ = 100 mg L^{-1}, C_{PMS} = 0.5 mM, $C_{Ethanol}$ or $C_{tert\text{-}BA}$ = 500 mM, $C_{p\text{-}BQ}$ = 50 mM.

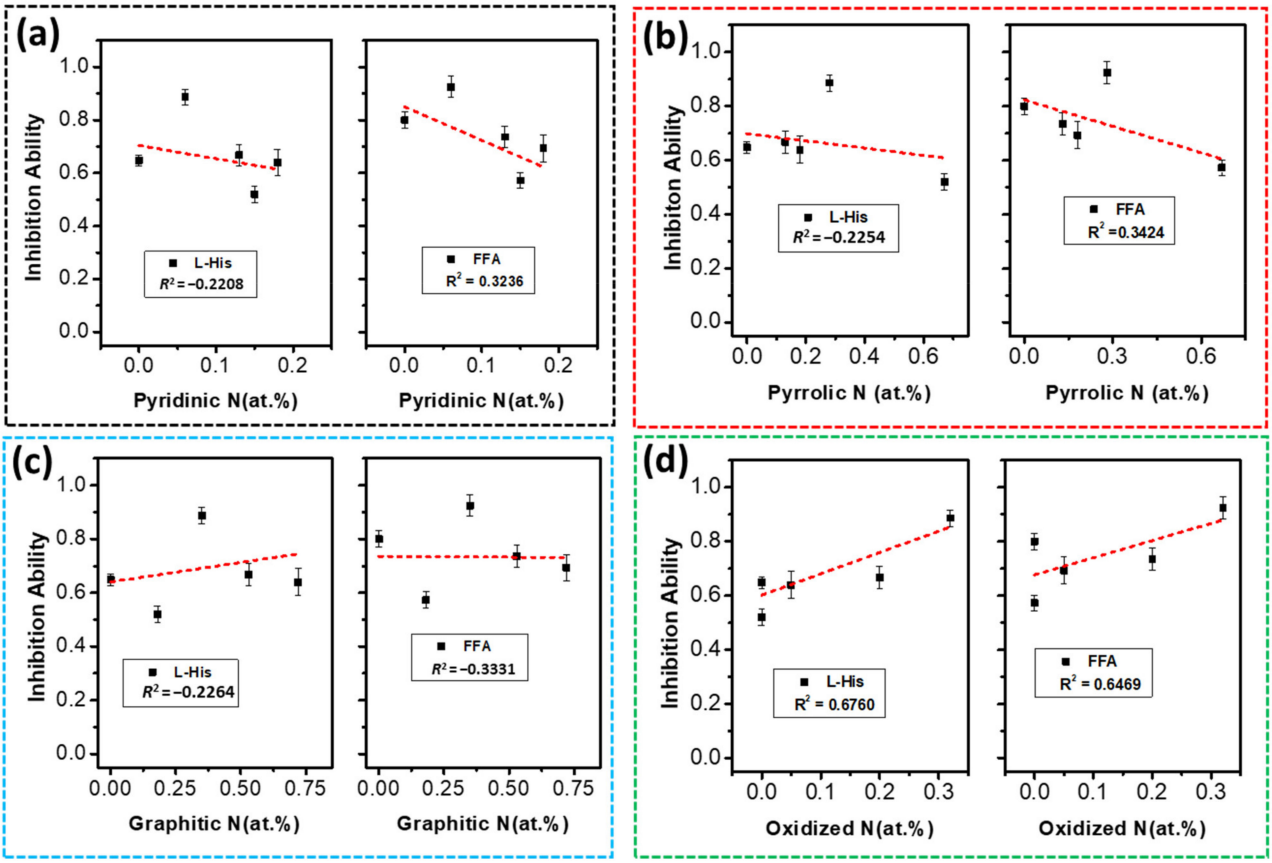

Figure 6. Role of singlet oxygen ($^1O_2$) quenchers on ACP degradation rate (k_1(ACP)). Correlation between k_1 (ACP) and pyridinic N (**a**), k_1 (ACP) and pyrrolic N (**b**), k_1 (ACP) and graphitic N (**c**), and k_1 (ACP) and oxidized N (**d**). Quenching studies were carried out at C_{ACP} = 10 mg L^{-1}, $C_{Catalyst}$ = 100 mg L^{-1}, C_{PMS} = 0.5 mM, C_{FFA} = $C_{L\text{-}His}$ = 50 mM.

Interestingly, the oxidized N exhibited meaningful correlation of R^2 = 0.6760 and R^2 = 0.6469 with L-His and FFA, respectively (Figure 6d), while other N-dopants provided a low R^2 value with $^1O_2$ quenchers. This proposes that the oxidized N has an auxiliary role in the $^1O_2$ mediative oxidative pathway. The inhibition ability of the non-free radicals in Figure 7a showed a high correlation (R^2 = 0.8929) between $NaClO_4$ and pyridinic N, emphasizing that pyridinic N accelerates catalytic oxidation by electron-transfer-based oxidation.

It also shows a decent correlation with phenol (R^2 = 0.8901), suggesting that the surface-bound radicals were also controlled via boundary pyridinic N. Moreover, graphitic N also yields notable R^2 = 0.8572 (KI), which implies that graphitic N can form activated complexes (carbocatalyst-PMS*) and initiate the electron-transfer process (Figure 7c). The N-dopant non-free radical activity correlation indicates that pyridinic N delivers more electron density to the carbon periphery and improves electron conductivity in the carbon framework. It could propagate the non-radial oxidative pathway through the formation of surface-bound radicals. Moreover, graphitic N facilitates electron-transfer based oxidation preferentially via the formation of carbocatalyst-PMS* activated complexes. W. Ren and his co-workers demonstrated that N-doped CNT profoundly enhances the PMS adsorption quantity and forms NCNT-PMS* complexes, which significantly raised the phenol oxidation efficiency through the electron-transfer regime [34].

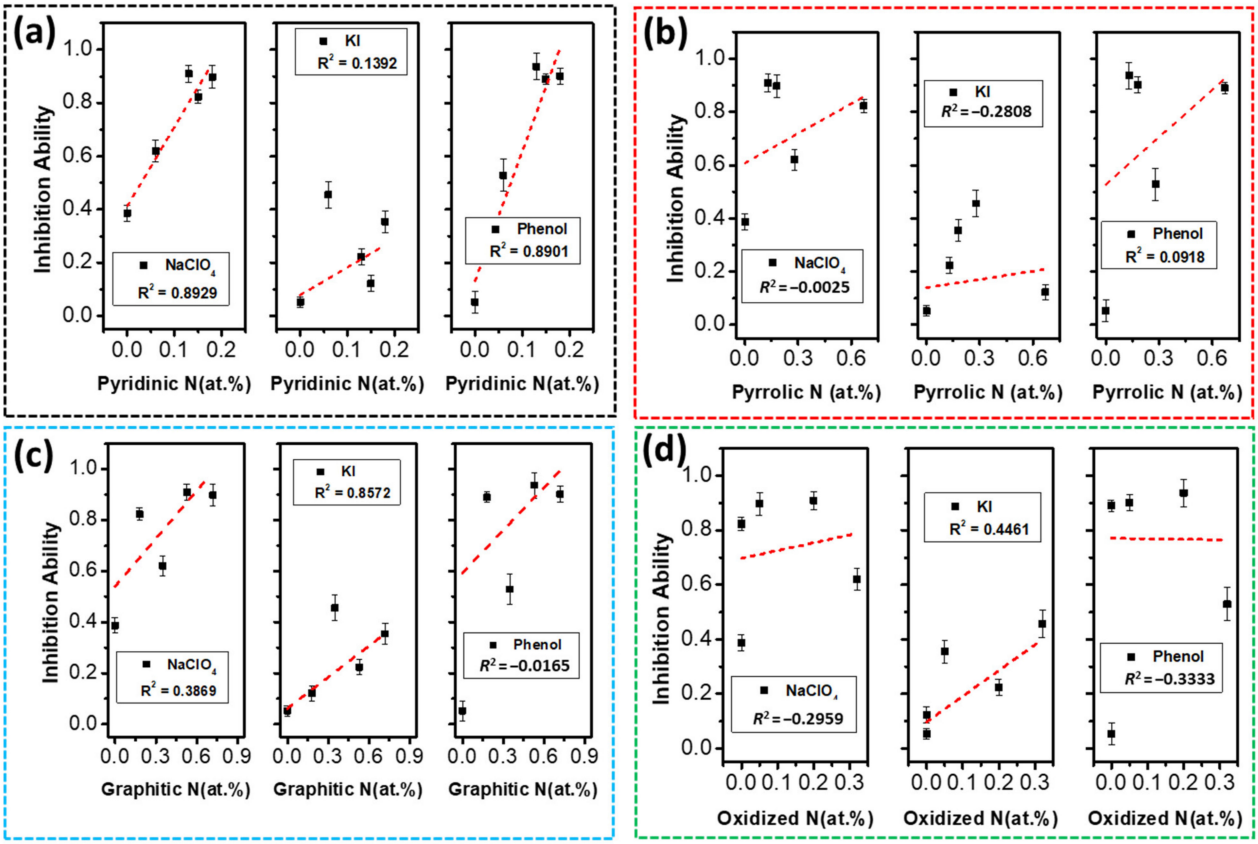

Figure 7. Role of non-radical (free electrons, surface-bound •OH and $SO_4^{\bullet -}$ radicals and surface-bound activated complexes) quenchers on ACP degradation (k_1(ACP)). Correlation between k_1 (ACP) and pyridinic N (**a**), k_1 (ACP) and pyrrolic N (**b**), k_1 (ACP) and graphitic N (**c**), and k_1 (ACP) and oxidized N (**d**). Quenching studies were carried out at C_{ACP} = 10 mg L^{-1}, $C_{Catalyst}$ = 100 mg L^{-1}, C_{PMS} = 0.5 mM, C_{FFA} = $C_{L\text{-}His}$ = 50 mM.

2.5.2. Role of O-Contents on Radical and Non-Radical Pathway

To investigate the oxygen functionalities–activity relationship, the normalized inhibition ability was correlated with O-contents. The obtained result was scrutinized alongside the individual oxygen functional groups and presented in Figure 8a–c. A good R^2 value is obtained between *p*-BQ and the carbonyl group (0.9827), while the hydroxyl group and carboxyl group yield very low R^2. This corroborates that a greater quantity of $O_2^{\bullet -}$ is produced with the increasing carbonyl content, highlighting that the carbonyl group crucially leads the $O_2^{\bullet -}$ -based oxidation. Furthermore, the inhibition ability of ethanol and *tert*-BA correlated with all the oxygen groups and showed no notable linear relationship (Figure 8b,c), implying that the $SO_4^{\bullet -}$/•OH-based oxidation pathway is not directly dependent on any specific oxygenated functional groups. The inhibition ability of L-His/FFA is also shown in Figure 9. Surprisingly, the negligible R^2 values of L-His/FFA with all the oxygen-containing functional group reveals that oxygen-containing functional groups did not directly govern the $^1O_2$ oxidation pathway. Figure 10b shows a high R^2 value with the carbonyl group (0.9472) and KI, suggesting that the -C=O group may play a major role in the surface-bound radical-based oxidation pathway. Furthermore, the hydroxyl group and carbonyl group exhibit a low R^2 value with KI, implying that -C-OH and COOH do not considerably regulate the surface-bound radicals (Figure 10a,c). On the other hand, the hydroxyl group provides a negative linear relationship with $NaClO_4$ (0.7485) and phenol (0.8932). It indicates that the presence of more electron-donating groups (-C-OH) could largely hinder the electron-transfer oxidative pathway, as well as attenuating the formation of NCNTs-PMS* activated complexes. This may be ascribed to the interplaying of oxygen functional groups and the fact that the primary carbon periphery adversely

affected the surface-activated complex mediative oxidative process [16,42,53]. This study also demonstrates that formation of more hydroxyl groups on graphitic layer deliberately interrupts the non-free radical pathway (electrons and surface-bound complex). This observation also matches with Figure 3a, which shows the oxygen functional groups–catalytic activity relationship.

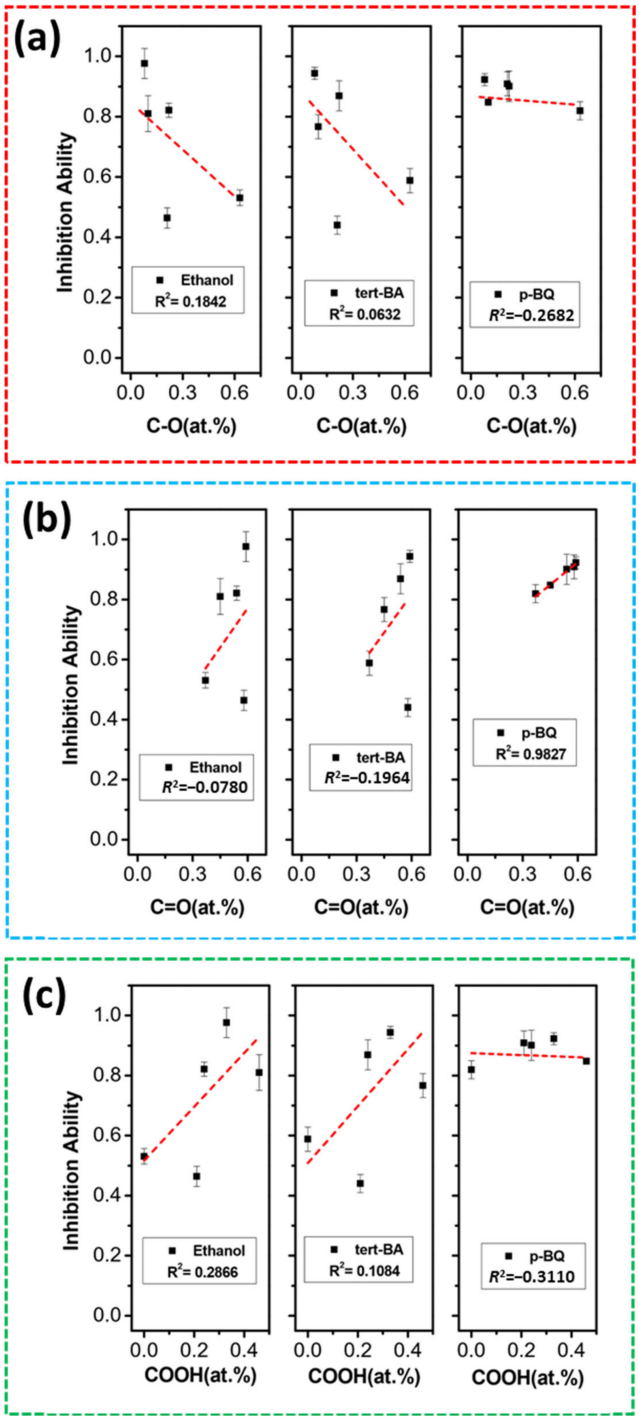

Figure 8. Role of radical ($O_2^{\bullet -}$-, $^{\bullet}OH$ and $SO_4^{\bullet -}$) quenchers on ACP degradation rate (k_1). Correlation between k_1 -C-O (**a**), k_1 and -C=O (**b**) and k_1 and -COOH (**c**). Quenching studies were carried out at C_{ACP} = 10 mg L^{-1}, $C_{Catalyst}$ = 100 mg L^{-1}, C_{PMS} = 0.5 mM, $C_{Ethanol}$ or $C_{tert\text{-}BA}$ = 500 mM, $C_{p\text{-}BQ}$ = 50 mM.

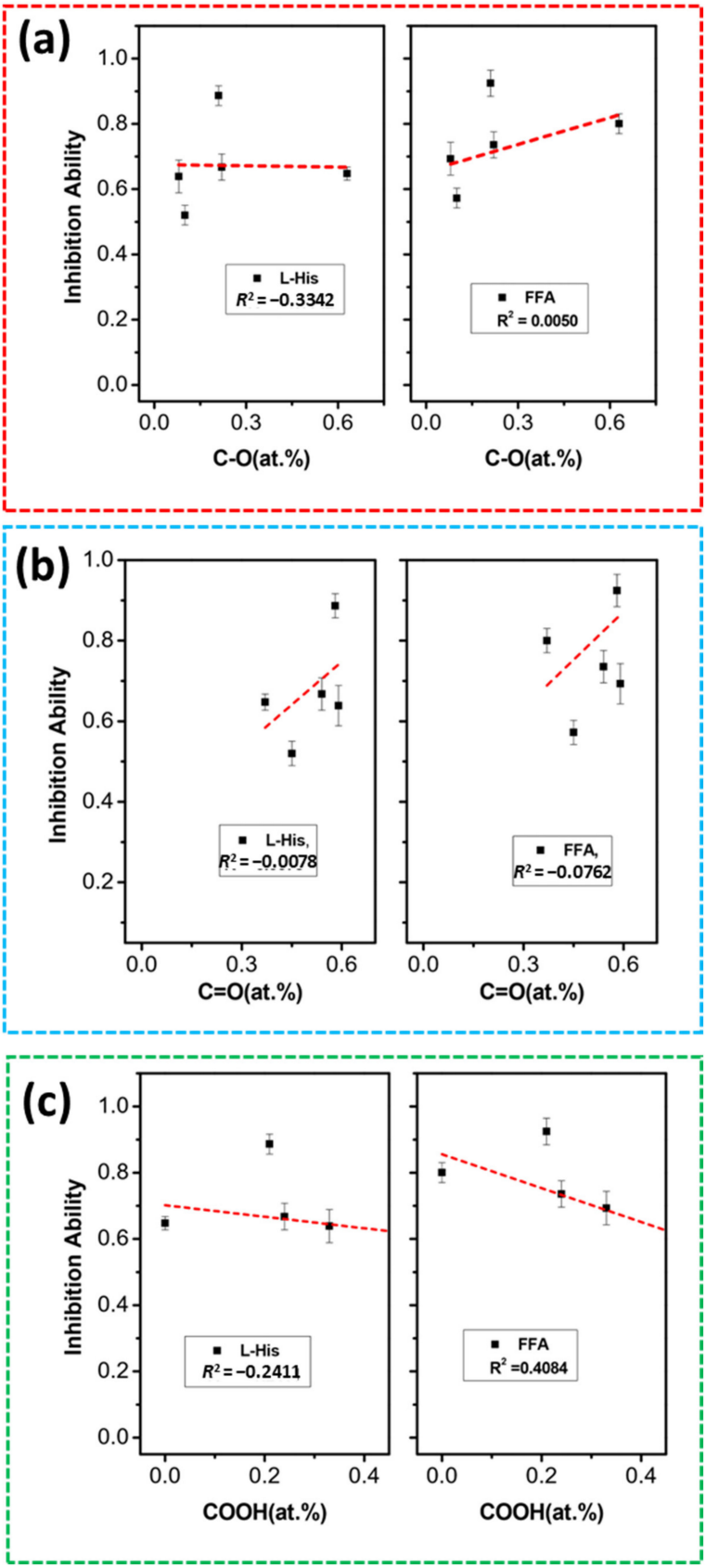

Figure 9. Role of singlet oxygen ($^1O_2$) on ACP degradation rate (k_1). Correlation between k_1 and -C-O (**a**), k_1 and -C=O (**b**) and k_1 and -COOH (**c**). Quenching studies were carried out at C_{ACP} = 10 mg L^{-1}, $C_{Catalyst}$ = 100 mg L^{-1}, C_{PMS} = 0.5 mM, C_{FFA} = $C_{L\text{-}His}$ = 50 mM.

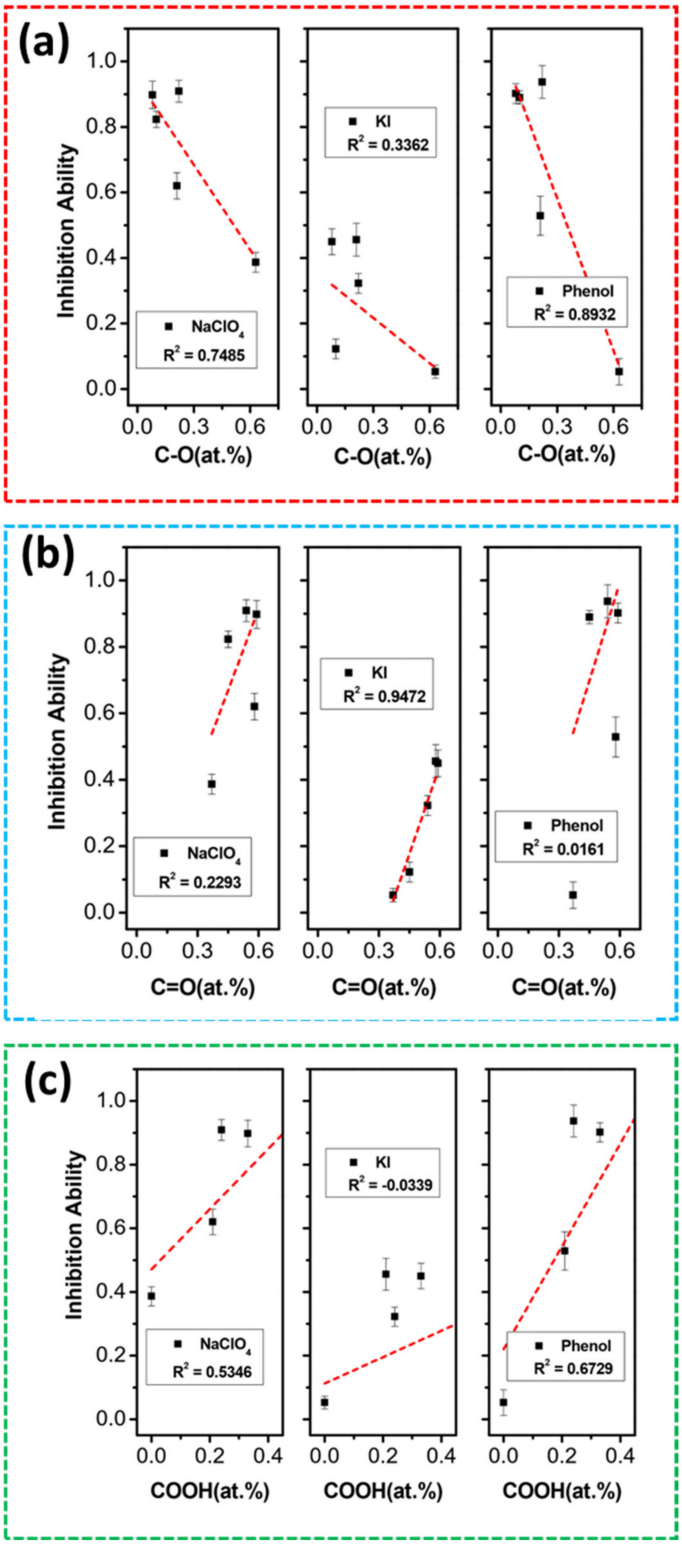

Figure 10. Role of non-radical (free electrons, surface-bound radicals ($^{\bullet}OH$ and $SO_4^{\bullet -}$) and surface-bound activated complex) quenchers on ACP degradation rate (k_1). Correlation between k_1 -C-O (**a**), k_1 and -C=O (**b**) and k_1 and -COOH (**c**). Quenching studies were carried out at C_{ACP} = 10 mg L^{-1}, $C_{Catalyst}$ = 100 mg L^{-1}, C_{PMS} = 0.5 mM, C_{FFA} = $C_{L\text{-}His}$ = 50 mM.

2.6. Insights into NCNTs/PMS and Unveiling the Active Sites

The catalytic performance of nitrogen-doped CNTs is fundamentally determined by their intrinsic electronic configurations (sp^2- and sp^3- hybridization). N-groups and

the oxygen-containing functional groups, and the structural defects (edges and vacancies) are believed to be key active sites for catalytic oxidation [32–37]. This present catalytic system demonstrates that high catalytic activity is noticed with Uz-NCNT-4/PMS (k_1(ACP) = 28.35 × 10^{-4} s^{-1}), rather than pristine CNT, NCNT, Uz-NCNT-2 and Uz-NCNT-4. The summary of the structure–catalytic activity regression analysis (Table S6) affirms that pyridinic N and graphitic N groups are major active sites for high catalytic oxidation. Thus, the presence of a high content of pyridinic N (0.18 at. %) and graphitic N (0.72 at. %) with Uz-NCNT-4 shows high catalytic activity. This hypothesis also matched with the structure–catalytic activity by the specific reactive species relationship, as depicted in Table 3. The assessment demonstrates that pyridinic N, as well as substitutional N (graphitic N), cooperatively lead the catalytic oxidation through radical as well as non-radical pathways.

Table 3. Role of N-dopants and oxygen functional groups on carbocatalyst/PMS activation pathway.

Carbocatalyst/PMS Activation Pathway	Reactive Oxidative Species	Governing N-Dopants	Correlation Coefficient (R^2)	Governing O-Groups	Correlation Coefficient (R^2)
Radical Species	$^{\bullet}OH/SO_4^{\bullet -}$	Pyridinic N	0.7359 (Ethanol) 0.7309 (*tert*-BA)	—	—
	$O_2^{\bullet -}$	Graphitic N	0.9259 (*p*-BQ)	-C=O	0.9827 (*p*-BQ)
Singlet Oxygen	$^1O_2$	—	—	—	—
Non-Radical Species	Free flowing electrons	Pyridinic N	0.8929 ($NaClO_4$)	-C-O	0.7485 ($NaClO_4$) (Downtrend)
	Surface-bound radicals	Graphitic N	0.8572 (KI)	-C=O	0.9472 (KI)
	Carbocatalyst-PMS* activated complex	Pyridinic N	0.8901 (Phenol)	-C-O	0.8932 (Phenol) (Downtrend)

The sp^2-hybridized N atom in a six-membered pyridinic ring is typically produced at the edges and defects of the main graphitic network and provides one p-electron to the conjugated π system. Consequently, pyridinic N can increase the density of π states of the graphitic network, which can facilitate the notable electron-transfer oxidative pathway (Figure 11a). Pyridinic N activity-inhibition ability with $NaClO_4$ correlation (R^2 = 0.8929, Table 3) supports this assumption. It means that the free flowing π electrons from sp^2-C in the graphitic carbon network can be activated through conjugating with the lone-pair electrons of pyridinic N [16]. The detectable R^2 value of pyridinic N with ethanol/*tert*-BA recommends that the terminal and edges of pyridinic N may also help to generate $SO_4^{\bullet -}$/$^{\bullet}OH$ through the interaction between the O-O bond of HO-O-SO_3^- and pyridinic N (Figure 11b). Luo and coworkers suggested that pyridinic N with a lone pair electron can significantly improve the π conjugation [52]. Graphitic N can also be another key active site, as shown in this study. The smaller atomic radius and high electronegativity graphitic N (3.04) compared to the adjacent carbon atoms (2.55) can stretch the electrons from neighboring carbon atoms [34]. These activated carbon centers can potentially interact with HO-O-SO_3^- to form a highly reactive complex (NCNT–PMS*) via the direct electron-abstraction step and generate surface-confined free radicals on the catalyst surface (Figure 11c). This hypothesis is witnessed from the correlation between graphitic N-inhibition ability by KI (R^2 = 0.8572, Table 3). Structure–oxidative species activity also substantiates that graphitic N can induce the radical pathway via $O_2^{\bullet -}$ in the catalytic system (Figure 11e).

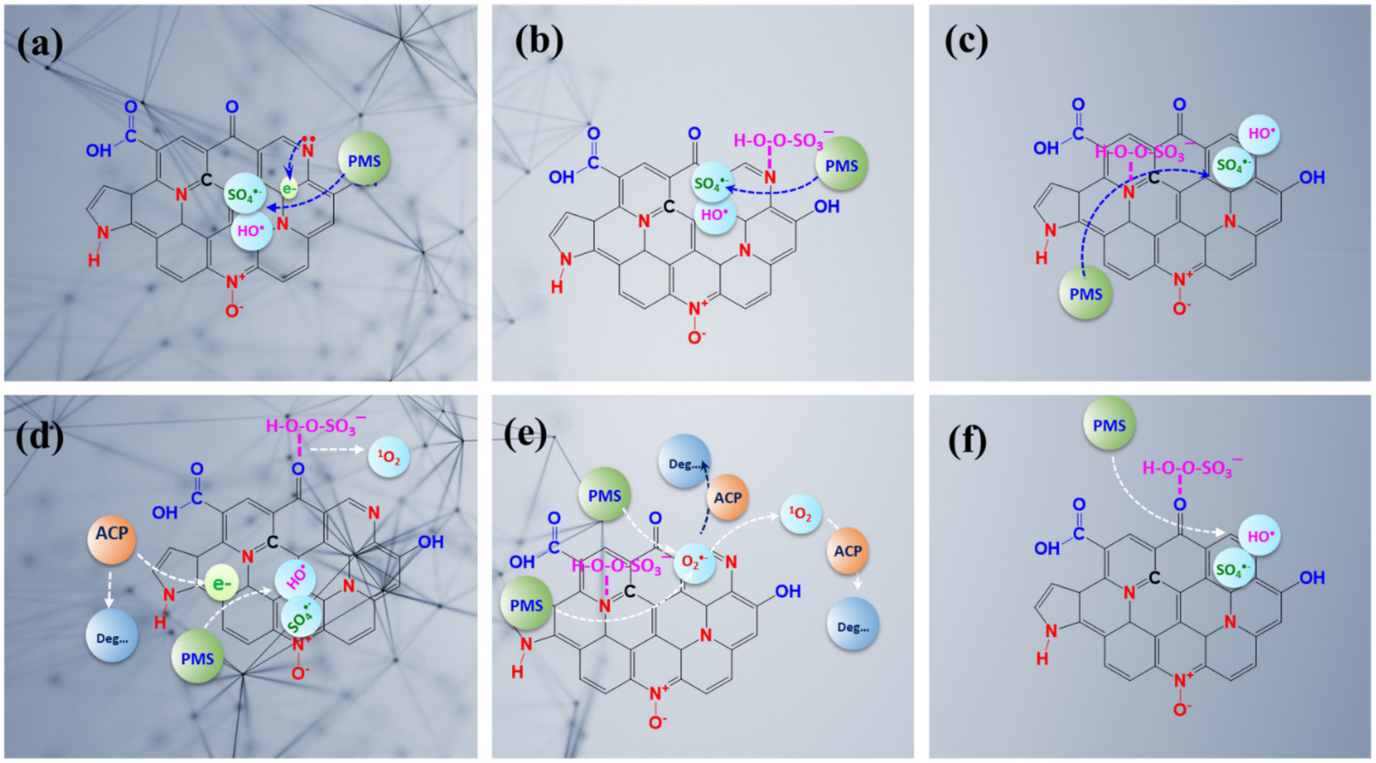

Figure 11. Proposed mechanism in PMS activation by NCNTs, non-radical pathway (**a**–**d**) and radical pathway (**e**–**f**).

Uz-NCNT-4 with the highest content of carbonyl groups (0.59 at. %), along with low contents of the hydroxyl group (0.08 at. %), shows superior catalytic performances. Tables S6 and 3 show that the carbonyl group can act as the principal active site rather than the other oxygen-containing functional groups. The electron-rich carbonyl group can act as an electron donor. Thus, the electrophilic group (peroxide bond) in PMS can be activated with the nucleophilic carbonyl group by electron-transfer and then produces reactive free radicals (Figure 11d–f). A high R^2 value (0.9427) between KI and the carbonyl group affirms that electron transfer between PMS and the carbonyl group can form surface-bound radicals. These electron-transfer processes and active surface-confined free radicals perform remarkable catalytic oxidation. J. Li and co-workers revealed that nucleophilic carbonyl groups can provoke a redox cycle to produce $SO_4^{\bullet -}$/•OH [26].

Furthermore, the abundant hydroxyl group can relay a contrary role to catalytic oxidation. This may be explained by the fact that the electrophilic O-O group in PMS can be readily adsorbed with the electron-rich hydroxyl group [34]. Because the H atom in the hydroxyl group dissociates itself and binds with the PMS molecule, the electron transfer process is relatively low; thus, -C-OH in the graphitic network can convert to -C=O. This functional group conversion step may unfeasible for efficient PMS activation, as reported from the experimental observation with graphene-catalyzed PMS by X-Duan et.al [74]. The present study also substantiates that there is no good correlation between the $^1O_2$ quencher and the N-groups or O-groups, suggesting that N-dopants/oxygen-containing functional groups do not directly initiate the $^1O_2$. However, the EPR results show that $^1O_2$ is intrinsically produced in the catalytic system (Figure 3a). Typically, the formation of $^1O_2$ can include different pathways, including self-decomposition of PMS, the electron-transfer reaction from carbocatalyst to PMS and the coupling or direct oxidation of $O_2^{\bullet -}$ [9,75]. In addition, the detectable R^2 value with the carboxyl group (Figures 3b and 10c) indicates that non-bonded lone pair electrons in oxygen atoms in the carboxyl group can partially support the electron-transfer process for catalytic activity. Overall, Tables 3 and S6 clearly

demonstrate that N-doping and oxygen functional groups synergistically contribute to the radical and non-radical formation and ACP degradation process.

2.7. Activity Stability Test

To determine the activity stability of the carbocatalysts, the carbocatalysts were evaluated through a reusability test over three consecutive runs and this is depicted in Figure S8. Around 53, 94, 96, 99, and 96% of ACP degradation efficiency was observed with CNT, NCNT, Uz-NCNT-2, Uz-NCNT-4 and Uz-NCNT-8, respectively. However, approximately <5% of ACP degradation efficiency was reduced at the 3rd cycle. The deactivation of the carbocatalyst may be due to the intricate influences of surface characteristics and structural changes, including the adsorption of intermediates/by-products, coverage of active sites and loss of a small quantity of catalyst during filtration/separation. This phenomenon can inhibit the charge transfer process between the carbocatalyst and PMS, resulting in suppressed ACP oxidation [46]. Furthermore, Uz-NCNT-4 demonstrated a high ACP degradation efficiency with all runs compared to the other catalyst, confirming that the chemical oxidation of NCNT with 4 g $KMnO_4$ could remarkably improve the reusability and stability.

3. Materials and Methods

3.1. Materials

PMS (available as Oxone, $KHSO_5 \cdot 0.5KHSO_4 \cdot 0.5K_2SO_4$), dicyandiamide (99.5%, $C_2H_4N_4$), ethyl alcohol (99.5%, C_2H_5OH), phosphoric acid (85%, H_3PO_4), sulfuric acid (Conc. H_2SO_4), hydrogen peroxide (30%, H_2O_2) solution and sodium hydroxide (NaOH) were purchased from Sigma Aldrich, Seoul, South Korea. In addition, HPLC grade methanol (99%, CH_3OH) for HPLC was purchased from Honeywell, Seoul, South Korea. Pristine multiwalled carbon nanotubes (MWCNT), with a diameter of 5–15 nm and length of ~10 μm, were obtained from Carbon Nano-Materials Technology Co., Ltd., Seoul, South Korea. All chemicals were laboratory grade and were used without further purifications.

3.2. Preparation of NCNT and Uz-NCNTs with Different Degree of Oxidation

First, 1 g of pristine CNT powder and 0.48 g dicyandiamide were dispersed into 100 mL ethanol solution. The solution mixture was constantly stirred at 80 °C until the solution was evaporated to obtain a homogeneous mixture. The mixture was kept into a tubular furnace and pyrolyzed for 3 h at 600 °C under N_2 atmosphere, with a gas flow rate of 20 mL min^{-1}. After cooling down to room temperature, the obtained powder was sufficiently ground and labelled as NCNT. Later, an unzipped NCNT (Uz-NCNT) carbocatalyst was synthesized based on a previously reported chemical oxidation method [39,40]. Then, 1 g of as-prepared NCNT was dispersed into 100 mL of concentrated H_2SO_4 solution for 1 h, then 20 mL of H_3PO_4 was slowly added to the above mixture and continuously stirred in an oil bath at 80 °C. Subsequently, a desirable amount of oxidizing agent $KMnO_4$ was slowly introduced, and the reaction mixture was left to react for 2 h. Later, the warm reaction mixture was carefully transferred into 500 mL of cold water containing 15 mL of H_2O_2. Then, the solution was centrifuged, washed with dilute HCl solution and again 3–5 times with distilled water. Finally, the obtained precipitates were dried by freeze-drying. Different degrees of oxidized unzipped NCNT carbocatalyst named as Uz-NCNT-2, Uz-NCNT-4 and Uz-NCNT-8 were synthesized by varying the amount of oxidizing agent $KMnO_4$ with 2, 4 and 8 g, respectively.

3.3. Characterizations of Carbocatalyst

Surface functional groups of the carbocatalyst were analyzed using Fourier-transform infrared spectroscopy (FT-IR) on a PerkinElmer instrument (Spectrum One System, PerkinElmer, Waltham, MA, USA). UV-visible spectra were recorded using a UV-Visible spectrometer (UV 1240, Shimadzu, Kyoto, Japan). N_2 adsorption/desorption was measured by BELSORP-max, BEL, Japan, Inc., Tokyo, Japan. The Brunauer-Emmett-Teller (BET)

equation and Barrett-Joyner-Halenda (BJH) method was applied to determine the specific surface area and pore size distribution of the carbocatalyst, respectively. X-ray diffraction (XRD) patterns were obtained on a D8-Advanced diffractometer system from Bruker (Bruker, Karlsruhe, Germany) with kα radiation (λ = 1.5418 Å). The interlayer distance of the graphitic plane was determined by Bragg's equation, $n\lambda = 2d\sin\theta$, where λ is the incident wavelength (1.5406 Å), θ is the peak position, n is the order of diffraction (1), and d is the interlayer spacing or d-spacing value. Surface composition of the catalyst was examined with a K-Alpha TM X-ray photoelectron spectrometer (XPS) system (Thermo Electron, Waltham, MA, USA).

3.4. Evaluation of Catalytic Performance

Acetaminophen (ACP, $C_8H_9NO_2$, 151.16 g mol^{-1}) degradation tests were carried out to explore the catalytic performance of the NCNT and Uz-NCNTs regarding PMS activation. A total of 100 mg L^{-1} of carbocatalyst was added to 100 mL of ACP solution (10 mg L^{-1}) and stirred constantly (500 rpm) under dark conditions. At a given interval, 3 mL of solution was taken and filtered with a 0.22 μm pore size PVDF membrane filter. The concentration of ACP was analyzed using high-performance liquid chromatography (HPLC, Ultimate 3000, Dionex, Thermo Fisher Scientific, Waltham, MA, USA) with UV absorbance at 230 nm. The reverse-based separation was carried out on an Eclipse XDB-C18 analytical column (Eclipse Plus, 4.6 × 250 mm, 5 μm, Agilent, Santa Clara, CA, USA). The mobile phase was prepared with methanol and deionized water (1:2, *v:v*), and the mixed solution was adjusted by phosphoric acid until the pH reached 3. The flow rate, temperature, and injected volume were 0.8 mL min^{-1}, 25 °C, and 25 μL, respectively. All kinetic catalytic experiments were performed in triplicate and the relative standard errors were less than 5%.

The first-order kinetic equation was used and expressed as $-\ln(C_t/C_0) = k_1 t$, where k_1 represents the apparent rate constant (s^{-1}), and C_0 and C_t are the initial concentration (mg L^{-1}) and concentration at time t of ACP in solution, respectively [25]. The PMS concentration was also measured by KI, Na_2HCO_3, and a UV–Vis spectrophotometer (UV 1240, Shimadzu, Tokyo, Japan) [41]. The yellow color developed by the reaction between PS and iodide in the presence of bicarbonate exhibits an absorbance at 395 nm. PMS decomposition rate was also determined using first order kinetics. Moreover, the activity stability of the carbocatalyst was also determined by reusability tests with four consecutive steps.

3.5. Evolution of Reactive Species Quenching Study and EPR Analysis

Ethanol (C_5H_5OH), *tert*-butyl alcohol (*tert*-BA, $(CH_3)_3OH$), *para*-benzoquinone (*p*-BQ, $C_6H_4O_2$), furfuryl alcohol (FFA, $C_5H_6O_2$), L-histidine (L-His, $C_6H_9N_3O_2$), potassium iodide (KI), phenol (C_6H_5OH), and sodium perchlorate ($NaClO_4$) were employed to detect the reactive oxidative species involved in the reaction. Furthermore, electron spin resonance spectra were observed with a JES-FA200 (Joel, Tokyo, Japan, X-band) at ambient temperature under visible light irradiation (λ > 420 nm), using 5,5-dimethyl-1-pyrroline-*N*-oxide (DMPO) and 2,2,6,6-tetramethyl-4-pi-peridone (TMP) as the spin trapping agents.

4. Conclusions

Different levels of oxidized nitrogen-doped CNTs (Uz-NCNTs) were synthesized by varying the oxidizing agent $KMnO_4$. The specific surface area substantially decreased with increasing oxidation levels of N-doped CNT. On the other hand, the amount of oxygen 0.89 at. % (CNT) evidently increased to 3.04, 21.5, 24.58, and 32.16 at. % with NCNT, Uz-NCNT-2, Uz-NCNT-4 and Uz-NCNT-8, respectively. Catalytic performance of the carbocatalyst was examined via PMS activation for ACP degradation. Uz-NCNT-4 exhibited high catalytic activity for ACP degradation through PMS activation with a 6.5-fold enhancement, compared to the CNT activity.

The structure–catalytic activity relationship exposes the fact that pyridinic N and carbonyl groups play a key role in the catalytic system. EPR and classical quenching studies reveal that the radical ($SO_4^{\bullet -}$, $^{\bullet}OH$ and $O_2^{\bullet -}$), $^1O_2$ and non-radical species (surface-bound radical, electrons, and surface-bound complex) intrinsically contribute to catalytic oxidation. The mechanism of PMS activation on the carbocatalyst was illustrated based on the structure-oxidative species activity correlation. N-doping and oxygen-containing functional groups propagate both radial and non-radical mediative oxidation pathways. Existence of electron rich Pyridinic N and graphitic N configuration can boost up the greater electron density of the graphitic network and lead to significant electron transfer-based oxidation via surface-bound radicals. Moreover, the quantity of $O_2^{\bullet -}$ generation is steadily raised with the increase in graphitic N and the carbonyl group. A large amount of oxygen-containing functional groups greatly inhibits the $SO_4^{\bullet -}/^{\bullet}OH$ mediative oxidation pathway. The linear regression analysis also emphasized that the presence of more hydroxyl groups might be unfavorable for catalytic activity.

Supplementary Materials: The following supporting information can be downloaded at: https://www.mdpi.com/article/10.3390/catal12080845/s1, Figure S1: (a) XRD patterns and (b) Raman spectrum of CNT, NCNT and unzipped NCNTs; Figure S2: (a) UV-visible spectrum and (b) FT-IR spectrum of CNT, NCNT and unzipped NCNTs; Figure S3: BET N_2 adsorption/desorption profile of (a) CNT, (b) NCNT, (c) Uz-NCNT-2, (d) Uz-NCNT-4, (e) Uz-NCNT-8 and (f) BJH pore diameter.; Figure S4: (a) XPS survey spectrum, (b) N 1s core-level spectra, deconvoluted N 1s core-level spectra of (c) NCNT, (d) Uz-NCNT-2, (e) Uz-NCNT-4 and (f) Uz-NCNT-8; Figure S5: (a) C 1s spectra, and deconvoluted O 1s core-level spectra of (b) NCNT, (c) Uz-NCNT-2, (d) Uz-NCNT-4 and (e) Uz-NCNT-8; Figure S6: (a) Effect of various chemical quenchers on normalized ACP concentration at (a) CNT/PMS, (b) NCNT/PMS, (c) Uz-NCNT-2/PMS, (d) Uz-NCNT-4/PMS and (e) Uz-NCNT-8/PMS systems. Quenching studies were performed with C_{ACP} = 10 mg L^{-1}, $C_{Catalyst}$ = 100 mg L^{-1}, C_{PMS} = 0.5 mM, $C_{Ethanol}$ or $C_{tert\text{-}BA}$ = $C_{p\text{-}BQ}$ = 500 mM or C_{FFA} = $C_{L\text{-}His}$ = C_{NaClO4} = C_{phenol} C_{KI} = 50 mM; Figure S7: Impact of chemical scavengers on k_1 (ACP) under different catalytic systems. Quenching studies were carried out at C_{ACP} = 10 mg L^{-1}, $C_{Catalyst}$ = 100 mg L^{-1}, C_{PMS} = 0.5 mM, $C_{Ethanol}$ or $C_{tert\text{-}BA}$ = $C_{p\text{-}BQ}$ = 500 mM or C_{FFA} = $C_{L\text{-}His}$ = C_{NaClO4} = C_{phenol} = C_{KI} = 50 mM; Figure S8: ACP degradation efficiency by reusability test in three consecutive runs. Experimental conditions C_{ACP} = 10 mg L^{-1}, $C_{Catalyst}$ = 100 mg L^{-1}, C_{PMS} = 0.5 mM and $pH_0 = 7 \pm 0.3$; Table S1: Summary of N-doped CNT and proposed mechanistical pathway; Table S2: Details of Raman spectra and I_D/I_G ratio; Table S3: BET surface area and BJH pore diameter of derived carbocatalysts; Table S4: Atomic percentage of N-dopants in carbocatalysts was determined from N 1s spectra; Table S5: Atomic percentage of oxygen containing functional groups in carbocatalysts was determined from O 1s spectra; Table S6: Summary of key active sites in carbocatalyst/PMS activation for ACP degradation.

Author Contributions: Conceptualization and methodology, K.G.; validation and formal analysis, D.-G.K. and S.-O.K.; investigation, resources, data curation and writing—original draft preparation, K.G.; writing—review and editing, D.-G.K. and S.-O.K.; visualization and supervision, S.-O.K.; project administration, and funding acquisition, S.-O.K. All authors have read and agreed to the published version of the manuscript.

Funding: This work was supported by a National Research Foundation of Korea (NRF) grant funded by the Korean government (MSIT) (No. 2022R1A2B5B02001584).

Data Availability Statement: The data presented in this study are available upon request from the corresponding author.

Conflicts of Interest: The authors declare that they have no known competing financial interests or personal relationships that could have appeared to influence the work reported in this paper.

References

1. Oyekunle, D.T.; Zhou, X.; Shahzad, A.; Chen, Z. Review on Carbonaceous Materials as Persulfate Activators: Structure-Performance Relationship, Mechanism and Future Perspectives on Water Treatment. *J. Mater. Chem. A* **2021**, *9*, 8012–8050. [CrossRef]
2. Gao, Y.; Wang, Q.; Ji, G.; Li, A. Degradation of Antibiotic Pollutants by Persulfate Activated with Various Carbon Materials. *Chem. Eng. J.* **2022**, *429*, 132387. [CrossRef]
3. Wu, S.; Yu, L.; Wen, G.; Xie, Z.; Lin, Y. Recent Progress of Carbon-Based Metal-Free Materials in Thermal-Driven Catalysis. *J. Energy Chem.* **2021**, *58*, 318–335. [CrossRef]
4. Huang, W.; Xiao, S.; Zhong, H.; Yan, M.; Yang, X. Activation of Persulfates by Carbonaceous Materials: A Review. *Chem. Eng. J.* **2021**, *418*, 129297. [CrossRef]
5. Chen, Y.; Wei, J.; Duyar, M.S.; Ordomsky, V.V.; Khodakov, A.Y.; Liu, J. Carbon-Based Catalysts for Fischer-Tropsch Synthesis. *Chem. Soc. Rev.* **2021**, *50*, 2337–2366. [CrossRef]
6. Hu, H.; Du, Y.; Duan, X. Functional Materials for Eco-catalysis of Small Molecules. *EcoMat* **2021**, *3*, e12121. [CrossRef]
7. Huang, X.; Wu, S.; Xiao, Z.; Kong, D.; Liang, T.; Li, X.; Luo, B.; Wang, B.; Zhi, L. Predicting the Optimal Chemical Composition of Functionalized Carbon Catalysts towards Oxidative Dehydrogenation of Ethanol to Acetaldehyde. *Nano Today* **2022**, *44*, 101508. [CrossRef]
8. Ding, Y.; Wang, X.; Fu, L.; Peng, X.; Pan, C.; Mao, Q.; Wang, C.; Yan, J. Nonradicals Induced Degradation of Organic Pollutants by Peroxydisulfate (PDS) and Peroxymonosulfate (PMS): Recent Advances and Perspective. *Sci. Total Environ.* **2021**, *765*, 142794. [CrossRef]
9. Duan, X.; Sun, H.; Shao, Z.; Wang, S. Nonradical Reactions in Environmental Remediation Processes: Uncertainty and Challenges. *Appl. Catal. B Environ.* **2018**, *224*, 973–982. [CrossRef]
10. Hu, P.; Su, H.; Chen, Z.; Yu, C.; Li, Q.; Zhou, B.; Alvarez, P.J.J.; Long, M. Selective Degradation of Organic Pollutants Using an Efficient Metal-Free Catalyst Derived from Carbonized Polypyrrole via Peroxymonosulfate Activation. *Environ. Sci. Technol.* **2017**, *51*, 11288–11296. [CrossRef]
11. Zhang, T.; Zhu, H.; Croué, J.P. Production of Sulfate Radical from Peroxymonosulfate Induced by a Magnetically Separable CuFe2O4 Spinel in Water: Efficiency, Stability, and Mechanism. *Environ. Sci. Technol.* **2013**, *47*, 2784–2791. [CrossRef]
12. Anipsitakis, G.P.; Dionysiou, D.D.; Gonzalez, M.A. Cobalt-Mediated Activation of Peroxymonosulfate and Sulfate Radical Attack on Phenolic Compounds. Implications of Chloride Ions. *Environ. Sci. Technol.* **2006**, *40*, 1000–1007. [CrossRef]
13. Anipsitakis, G.P.; Stathatos, E.; Dionysiou, D.D. Heterogeneous Activation of Oxone Using Co_3O_4. *J. Phys. Chem. B* **2005**, *109*, 13052–13055. [CrossRef]
14. Wang, J.; Wang, S. Activation of Persulfate (PS) and Peroxymonosulfate (PMS) and Application for the Degradation of Emerging Contaminants. *Chem. Eng. J.* **2018**, *334*, 1502–1517. [CrossRef]
15. Liu, Y.; Wang, L.; Dong, Y.; Peng, W.; Fu, Y.; Li, Q.; Fan, Q.; Wang, Y.; Wang, Z. Current Analytical Methods for the Determination of Persulfate in Aqueous Solutions: A Historical Review. *Chem. Eng. J.* **2021**, *416*, 129143. [CrossRef]
16. Chen, X.; Oh, W.D.; Lim, T.T. Graphene- and CNTs-Based Carbocatalysts in Persulfates Activation: Material Design and Catalytic Mechanisms. *Chem. Eng. J.* **2018**, *354*, 941–976. [CrossRef]
17. Cheng, X.; Guo, H.; Zhang, Y.; Wu, X.; Liu, Y. Non-Photochemical Production of Singlet Oxygen via Activation of Persulfate by Carbon Nanotubes. *Water Res.* **2017**, *113*, 80–88. [CrossRef]
18. Liang, P.; Zhang, C.; Duan, X.; Sun, H.; Liu, S.; Tade, M.O.; Wang, S. An Insight into Metal Organic Framework Derived N-Doped Graphene for the Oxidative Degradation of Persistent Contaminants: Formation Mechanism and Generation of Singlet Oxygen from Peroxymonosulfate. *Environ. Sci. Nano* **2017**, *4*, 315–324. [CrossRef]
19. Yun, E.T.; Yoo, H.Y.; Bae, H.; Kim, H.I.; Lee, J. Exploring the Role of Persulfate in the Activation Process: Radical Precursor Versus Electron Acceptor. *Environ. Sci. Technol.* **2017**, *51*, 10090–10099. [CrossRef]
20. Lee, H.; Lee, H.J.; Jeong, J.; Lee, J.; Park, N.B.; Lee, C. Activation of Persulfates by Carbon Nanotubes: Oxidation of Organic Compounds by Nonradical Mechanism. *Chem. Eng. J.* **2015**, *266*, 28–33. [CrossRef]
21. Wang, X.; Qin, Y.; Zhu, L.; Tang, H. Nitrogen-Doped Reduced Graphene Oxide as a Bifunctional Material for Removing Bisphenols: Synergistic Effect between Adsorption and Catalysis. *Environ. Sci. Technol.* **2015**, *49*, 6855–6864. [CrossRef]
22. Duan, X.; Su, C.; Zhou, L.; Sun, H.; Suvorova, A.; Odedairo, T.; Zhu, Z.; Shao, Z.; Wang, S. Surface Controlled Generation of Reactive Radicals from Persulfate by Carbocatalysis on Nanodiamonds. *Appl. Catal. B Environ.* **2016**, *194*, 7–15. [CrossRef]
23. Lee, J.; Von Gunten, U.; Kim, J.H. Persulfate-Based Advanced Oxidation: Critical Assessment of Opportunities and Roadblocks. *Environ. Sci. Technol.* **2020**, *54*, 3064–3081. [CrossRef]
24. Pham, V.L.; Kim, D.G.; Ko, S.O. Catalytic Degradation of Acetaminophen by Fe and N Co-Doped Multi-Walled Carbon Nanotubes. *Environ. Res.* **2021**, *201*, 111535. [CrossRef]
25. Kim, D.G.; Ko, S.O. Advanced Oxidative Degradation of Acetaminophen by Carbon Catalysts: Radical vs Non-Radical Pathways. *Environ. Res.* **2020**, *188*, 109767.
26. Li, J.; Li, M.; Sun, H.; Ao, Z.; Wang, S.; Liu, S. Understanding of the Oxidation Behavior of Benzyl Alcohol by Peroxymonosulfate via Carbon Nanotubes Activation. *ACS Catal.* **2020**, *10*, 3516–3525. [CrossRef]
27. Duan, X.; Sun, H.; Wang, S. Metal-Free Carbocatalysis in Advanced Oxidation Reactions. *Acc. Res.* **2018**, *51*, 678–687. [CrossRef]

28. Duan, X.; Ao, Z.; Zhou, L.; Sun, H.; Wang, G.; Wang, S. Occurrence of Radical and Nonradical Pathways from Carbocatalysts for Aqueous and Nonaqueous Catalytic Oxidation. *Appl. Catal. B Environ.* **2016**, *188*, 98–105. [CrossRef]
29. Ma, W.; Wang, N.; Fan, Y.; Tong, T.; Han, X.; Du, Y. Non-Radical-Dominated Catalytic Degradation of Bisphenol A by ZIF-67 Derived Nitrogen-Doped Carbon Nanotubes Frameworks in the Presence of Peroxymonosulfate. *Chem. Eng. J.* **2018**, *336*, 721–731. [CrossRef]
30. Chen, J.; Zhang, L.; Huang, T.; Li, W.; Wang, Y.; Wang, Z. Decolorization of Azo Dye by Peroxymonosulfate Activated by Carbon Nanotube: Radical versus Non-Radical Mechanism. *J. Hazard. Mater.* **2016**, *320*, 571–580. [CrossRef]
31. Yan, Y.; Miao, J.; Yang, Z.; Xiao, F.X.; Yang, H.B.; Liu, B.; Yang, Y. Carbon Nanotube Catalysts: Recent Advances in Synthesis, Characterization and Applications. *Chem. Soc. Rev.* **2015**, *44*, 3295–3346. [CrossRef] [PubMed]
32. Guan, C.; Jiang, J.; Luo, C.; Pang, S.; Yang, Y.; Wang, Z.; Ma, J.; Yu, J.; Zhao, X. Oxidation of Bromophenols by Carbon Nanotube Activated Peroxymonosulfate (PMS) and Formation of Brominated Products: Comparison to Peroxydisulfate (PDS). *Chem. Eng. J.* **2018**, *337*, 40–50. [CrossRef]
33. Duan, X.; Sun, H.; Wang, Y.; Kang, J.; Wang, S. N-Doping-Induced Nonradical Reaction on Single-Walled Carbon Nanotubes for Catalytic Phenol Oxidation. *ACS Catal.* **2015**, *5*, 553–559. [CrossRef]
34. Ren, W.; Nie, G.; Zhou, P.; Zhang, H.; Duan, X.; Wang, S. The Intrinsic Nature of Persulfate Activation and N-Doping in Carbocatalysis. *Environ. Sci. Technol.* **2020**, *54*, 6438–6447. [CrossRef] [PubMed]
35. Sun, H.; Kwan, C.K.; Suvorova, A.; Ang, H.M.; Tadé, M.O.; Wang, S. Catalytic Oxidation of Organic Pollutants on Pristine and Surface Nitrogen-Modified Carbon Nanotubes with Sulfate Radicals. *Appl. Catal. B Environ.* **2014**, *154–155*, 134–141. [CrossRef]
36. Duan, X.; Ao, Z.; Sun, H.; Zhou, L.; Wang, G.; Wang, S. Insights into N-Doping in Single-Walled Carbon Nanotubes for Enhanced Activation of Superoxides: A Mechanistic Study. *Chem. Commun.* **2015**, *51*, 15249–15252. [CrossRef]
37. Wang, C.; Kang, J.; Liang, P.; Zhang, H.; Sun, H.; Tadé, M.O.; Wang, S. Ferric Carbide Nanocrystals Encapsulated in Nitrogen-Doped Carbon Nanotubes as an Outstanding Environmental Catalyst. *Environ. Sci. Nano* **2017**, *4*, 170–179. [CrossRef]
38. Yang, Q.; Chen, Y.; Duan, X.; Zhou, S.; Niu, Y.; Sun, H.; Zhi, L.; Wang, S. Unzipping Carbon Nanotubes to Nanoribbons for Revealing the Mechanism of Nonradical Oxidation by Carbocatalysis. *Appl. Catal. B Environ.* **2020**, *276*, 119146. [CrossRef]
39. Xiao, B.; Li, X.; Li, X.; Wang, B.; Langford, C.; Li, R.; Sun, X. Graphene Nanoribbons Derived from the Unzipping of Carbon Nanotubes: Controlled Synthesis and Superior Lithium Storage Performance. *J. Phys. Chem. C* **2014**, *118*, 881–890. [CrossRef]
40. Liu, M.; Song, Y.; He, S.; Tjiu, W.W.; Pan, J.; Xia, Y.Y.; Liu, T. Nitrogen-Doped Graphene Nanoribbons as Efficient Metal-Free Electrocatalysts for Oxygen Reduction. *ACS Appl. Mater. Interfaces* **2014**, *6*, 4214–4222. [CrossRef]
41. Wacławek, S.; Grübel, K.; Černík, M. Simple Spectrophotometric Determination of Monopersulfate. *Spectrochim. Acta Part A Mol. Biomol. Spectrosc.* **2015**, *149*, 928–933. [CrossRef]
42. Li, H.; Zhang, J.; Gholizadeh, A.B.; Brownless, J.; Fu, Y.; Cai, W.; Han, Y.; Duan, T.; Wang, Y.; Ling, H.; et al. Photoluminescent Semiconducting Graphene Nanoribbons via Longitudinally Unzipping Single-Walled Carbon Nanotubes. *ACS Appl. Mater. Interfaces* **2021**, *13*, 52892–52900. [CrossRef]
43. Chen, X.; Oh, W.D.; Hu, Z.T.; Sun, Y.M.; Webster, R.D.; Li, S.Z.; Lim, T.T. Enhancing Sulfacetamide Degradation by Peroxymonosulfate Activation with N-Doped Graphene Produced through Delicately-Controlled Nitrogen Functionalization via Tweaking Thermal Annealing Processes. *Appl. Catal. B Environ.* **2018**, *225*, 243–257. [CrossRef]
44. Chang, S.S.; Clair, B.; Ruelle, J.; Beauchêne, J.; Di Renzo, F.; Quignard, F.; Zhao, G.J.; Yamamoto, H.; Gril, J. Mesoporosity as a New Parameter for Understanding Tension Stress Generation in Trees. *J. Exp. Bot.* **2009**, *60*, 3023–3030. [CrossRef]
45. Groen, J.C.; Peffer, L.A.A.; Pérez-Ramírez, J. Pore Size Determination in Modified Micro- and Mesoporous Materials. Pitfalls and Limitations in Gas Adsorption Data Analysis. *Microporous Mesoporous Mater.* **2003**, *60*, 1–17. [CrossRef]
46. Duan, X.; Ao, Z.; Sun, H.; Indrawirawan, S.; Wang, Y.; Kang, J.; Liang, F.; Zhu, Z.H.; Wang, S. Nitrogen-Doped Graphene for Generation and Evolution of Reactive Radicals by Metal-Free Catalysis. *ACS Appl. Mater. Interfaces* **2015**, *7*, 4169–4178. [CrossRef]
47. Duan, X.; Indrawirawan, S.; Sun, H.; Wang, S. Effects of Nitrogen-, Boron-, and Phosphorus-Doping or Codoping on Metal-Free Graphene Catalysis. *Catal. Today* **2015**, *249*, 184–191. [CrossRef]
48. Krishnamoorthy, K.; Veerapandian, M.; Yun, K.; Kim, S.J. The Chemical and Structural Analysis of Graphene Oxide with Different Degrees of Oxidation. *Carbon* **2013**, *53*, 38–49. [CrossRef]
49. Dash, S.; Patel, S.; Mishra, B.K. Oxidation by Permanganate: Synthetic and Mechanistic Aspects. *Tetrahedron* **2009**, *65*, 707–739. [CrossRef]
50. Russ, M.T. Dimanganese Heptoxide for the Selective Oxidaion of Organic Substrates. *Angew. Chem. Int. Ed.* **1987**, *26*, 1007–1009.
51. Ma, Y.; Wu, X.; Yu, M.; Li, S.; Liu, J. Turning free-standing three dimensional graphene into electrochemically active by nitrogen doping during chemical vapor deposition process. *J. Mater. Sci. Mater. Electron.* **2020**, *31*, 3759–3768. [CrossRef]
52. Luo, Z.; Lim, S.; Tian, Z.; Shang, J.; Lai, L.; MacDonald, B.; Fu, C.; Shen, Z.; Yu, T.; Lin, J. Pyridinic N Doped Graphene: Synthesis, Electronic Structure, and Electrocatalytic Property. *J. Mater. Chem.* **2011**, *21*, 8038–8044. [CrossRef]
53. Ren, W.; Xiong, L.; Nie, G.; Zhang, H.; Duan, X.; Wang, S. Insights into the Electron-Transfer Regime of Peroxydisulfate Activation on Carbon Nanotubes: The Role of Oxygen Functional Groups. *Environ. Sci. Technol.* **2020**, *54*, 1267–1275. [CrossRef]
54. Frank, B.; Zhang, J.; Blume, R.; Schlögl, R.; Su, D.S. Heteroatoms Increase the Selectivity in Oxidative Dehydrogenation Reactions on Nanocarbons. *Angew. Chem. Int. Ed.* **2009**, *48*, 6913–6917. [CrossRef]
55. Frank, B.; Blume, R.; Rinaldi, A.; Trunschke, A.; Schlögl, R. Oxygen Insertion Catalysis by Sp2 Carbon. *Angew. Chem. Int. Ed.* **2011**, *50*, 10226–10230. [CrossRef]

56. Liu, S.; Peng, W.; Sun, H.; Wang, S. Physical and Chemical Activation of Reduced Graphene Oxide for Enhanced Adsorption and Catalytic Oxidation. *Nanoscale* **2014**, *6*, 766–771. [CrossRef]
57. Gao, Y.; Chen, Z.; Zhu, Y.; Li, T.; Hu, C. New Insights into the Generation of Singlet Oxygen in the Metal-Free Peroxymonosulfate Activation Process: Important Role of Electron-Deficient Carbon Atoms. *Environ. Sci. Technol.* **2020**, *54*, 1232–1241. [CrossRef]
58. Gao, Y.; Zhu, Y.; Chen, Z.; Zeng, Q.; Hu, C. Insights into the Difference in Metal-Free Activation of Peroxymonosulfate and Peroxydisulfate. *Chem. Eng. J.* **2020**, *394*, 123936. [CrossRef]
59. Tian, X.; Gao, P.; Nie, Y.; Yang, C.; Zhou, Z.; Li, Y.; Wang, Y. A Novel Singlet Oxygen Involved Peroxymonosulfate Activation Mechanism for Degradation of Ofloxacin and Phenol in Water. *Chem. Commun.* **2017**, *53*, 6589–6592. [CrossRef]
60. Tang, W.; Zhang, Y.; Guo, H.; Liu, Y. Heterogeneous Activation of Peroxymonosulfate for Bisphenol AF Degradation with BiOI0.5Cl0.5. *RSC Adv.* **2019**, *9*, 14060–14071. [CrossRef]
61. Kim, D.G.; Ko, S.O. Effects of thermal modification of a biochar on persulfate activation and mechanisms of catalytic degradation of a pharmaceutical. *Chem. Eng. J.* **2020**, *399*, 125377. [CrossRef]
62. Buxton, G.V.; Greenstock, C.L.; Helman, W.P.; Ross, A.B. Critical Review of Rate Constants for Reactions of Hydrated Electrons, Hydrogen Atoms and Hydroxyl Radicals (·OH/·O− in Aqueous Solution. *J. Phys. Chem. Ref. Data* **1988**, *17*, 513–886. [CrossRef]
63. Eibenberger, H.; Steenken, S.; O'Neill, P.; Schulte-Frohlinde, D. Pulse Radiolysis and Electron Spin Resonance. *J. Phys. Chem. C* **1978**, *82*, 749–750. [CrossRef]
64. Greenstock, C.L.; Ruddock, G.W. Determination of Superoxide (O2-) Radical Anion Reaction Rates Using Pulse Radiolysis. *Int. J. Radiat. Phys. Chem.* **1976**, *8*, 367–369. [CrossRef]
65. Manring, L.E.; Kramer, M.K.; Foote, C.S. Interception of O2- by Benzoquinone in Cyanoaromatic-Sensitized Photooxygenations. *Tetrahedron Lett.* **1984**, *25*, 2523–2526. [CrossRef]
66. Wilkinson, F.; Brummer, J.G. Rate Constants for the Decay and Reactions of the Lowest Electronically Excited Singlet State of Molecular Oxygen in Solution. *J. Phys. Chem. Ref. Data* **1981**, *10*, 809–999. [CrossRef]
67. Haag, W.R.; Hoigné, J. Singlet Oxygen in Surface Waters. 3. Photochemical Formation and Steady-State Concentrations in Various Types of Waters. *Environ. Sci. Technol.* **1986**, *20*, 341–348. [CrossRef]
68. Lindsey, M.E.; Tarr, M.A. Inhibition of Hydroxyl Radical Reaction with Aromatics by Dissolved Natural Organic Matter. *Environ. Sci. Technol.* **2000**, *34*, 444–449. [CrossRef]
69. Ziajka, J.; Pasiuk-Bronikowska, W. Rate Constants for Atmoshpheric Trace Organics Scavenging SO4- in the Fe-Catalysed Autoxidation of S(IV). *Atmos. Environ.* **2005**, *39*, 1431–1438. [CrossRef]
70. Lin, Y.; Sun, X.; Su, D.S.; Centi, G.; Perathoner, S. Catalysis by Hybrid Sp2/Sp3 Nanodiamonds and Their Role in the Design of Advanced Nanocarbon Materials. *Chem. Soc. Rev.* **2018**, *47*, 8438–8473. [CrossRef]
71. Buxton, G.V.; Elliot, A.J. Rate Constant for Reaction of Hydroxyl Radicals with Bicarbonate Ions. *Int. J. Radiat. Appl. Instrum. Part C* **1986**, *27*, 241–243. [CrossRef]
72. Liang, J.; Xu, X.; Qamar Zaman, W.; Hu, X.; Zhao, L.; Qiu, H.; Cao, X. Different Mechanisms between Biochar and Activated Carbon for the Persulfate Catalytic Degradation of Sulfamethoxazole: Roles of Radicals in Solution or Solid Phase. *Chem. Eng. J.* **2019**, *375*, 121908. [CrossRef]
73. Huang, Z.; Bao, H.; Yao, Y.; Lu, W.; Chen, W. Novel Green Activation Processes and Mechanism of Peroxymonosulfate Based on Supported Cobalt Phthalocyanine Catalyst. *Appl. Catal. B Environ.* **2014**, *154–155*, 36–43. [CrossRef]
74. Duan, X.; Sun, H.; Ao, Z.; Zhou, L.; Wang, G.; Wang, S. Unveiling the Active Sites of Graphene-Catalyzed Peroxymonosulfate Activation. *Carbon* **2016**, *107*, 371–378. [CrossRef]
75. Evans, D.F.; Upton, M.W. Studies on Singlet Oxygen in Aqueous Solution. Part 3. The Decomposition of Peroxy-Acis. *J. Chem. Soc. Dalton Trans.* **1985**, *6*, 1151–1153. [CrossRef]